Article

Design and Optimization of a Novel Compliant Z-Positioner for the Nanoindentation Testing Device

Minh Phung Dang * , **Thanh Dat Le, Hieu Giang Le and Chi Thien Tran**

Faculty of Mechanical Engineering, Ho Chi Minh City University of Technology and Education,
Ho Chi Minh City 700000, Vietnam
* Correspondence: phungdm@hcmute.edu.vn

Abstract: Compliant mechanisms are extensively utilized in precise positioning systems. This work presents a novel compliant fine Z-positioner for directing the indenter in a nanoindentation testing positioning system. Initially, the suggested positioner consists of a novel hybrid symmetric compliant displacement amplifier of four-lever and Scott Russell structures combined with a parallel guiding mechanism. Subsequently, a static–dynamic characteristic of the proposed positioner is modeled by the pseudo-rigid body method and the Lagrange technique. Based on the FEA results, the parasitic motion error of the developed fine Z-positioner was 0.0956%. Thirdly, the analytical result was verified by FEA analysis, and the error between the two methods was 0.5869%. Therefore, the proposed analytical approach was reliable for quickly assessing the output response of the proposed positioner. Finally, to enhance the quality of the proposed structure's response, the main design variables of the fine Z-positioner are optimized using the Firefly algorithm. The optimal findings indicated that the first natural frequency occurs at around 220.16 Hz. The imprecision between the optimal result and the FEA result was 9.67%. The analytical results are in close agreement with the confirmed FEA result. The prototype was manufactured by the computerized numerical milling method. The inexactness between the FEA outcome and the experimentation outcome was 11.04%. Based on the FEA and experiment results, displacement amplification proportions were 6.8725 and 8, respectively. In addition, the experimental results demonstrated a good linear relationship for guiding mechanisms in nanoindentation testing positioning systems.

Keywords: compliant mechanism; fine Z-positioner; static–dynamic analysis; precise positioning nanoindentation testing

1. Introduction

Compliant mechanisms utilize monolithic structures, eliminating backlash, friction, and the need for assembly, lubrication, and maintenance, while offering lightweight, compact sizes and lower costs [1,2]. Therefore, compliant mechanisms have been widely utilized in various fields, including constant-torque mechanisms [3], bistable mechanisms [4,5], assisted-vibration machining [6–8], micro grippers [9–11], harvesters for energy [12], robotics [13], and precise positioning [14–16]. Compliant mechanisms have been primarily utilized in precise positioning devices due to their high resolution, precisely repeatable motion, low friction, and compact size [17]. Therefore, based on the advantages of compliant mechanisms, they have been potentially utilized in compliant positioners for precise positioning systems as well as nanoindentation locating systems to locate the sample position for assessing the mechanical properties of biological specimens. Currently,

nanoindentation instruments exploit traditional instruments for real-time detection and observation of the mechanical characteristics of the specimen [18,19]. Therefore, a compact design is a potential application for an in situ nanoindentation checking system, aiming to reduce energy consumption and minimize working space. To locate accurately, in situ nanoindentation instruments frequently demand numerous force-displacement feedback sensors. In situ nanoindentation utilizes a fine Z-positioner to guide the indenter and a fine XY-positioner to locate the biological specimen accurately. However, the current positioners have a slow response and a low resonance frequency. Their size makes it challenging to integrate in situ nanoindentation with multi-microscopes into a scanning electron microscope (SEM). Therefore, an innovative compliant compact positioner with a rapid response and a suitable working stroke is essential for guiding the indenter integrated into the nanoindentation testing positioning system.

Series, parallel, or series-parallel configurations are the fundamental design principles applicable to the design of compliant positioners [20]. In general, because of the significant advantages of piezoelectric actuators (PEAs), including high stiffness, high response, and high load capacity, PEAs have been widely utilized for controlling the compliant positioners. Meanwhile, the working stroke of the PEA has limited travel. Hence, various displacement amplification structures have been developed for enhancing the working stroke of the PEA, including the lever mechanism [21], the bridge mechanism [19,22], the bridge-lever mechanism [23] and the double rocker mechanism [24]. Specifically, Wu et al. integrated a bridge displacement amplifier into a compact XY positioner, featuring a working stroke of 212.48×219.24 µm for accurate positioning [25]. Yang et al. progressed to an innovative flexure XY-platform integrated with a symmetric compliant double rocker displacement amplifier for a precise positioning system [24]. Wu et al. proposed a 2-dof positioner combined with a symmetric 2-lever displacement amplifier for accurate localization [22]. Kim et al. utilized a hybrid amplifier comprising two L-shaped levers integrated with circular and cartwheel hinges in the compliant XYθ positioner for precise rotary positioning [26]. Cheng et al. developed a new compliant XY positioner with a hybrid double-floor bridge displacement mechanism for micro/nano manipulations [27]. Choi et al. combined a double-floor lever amplifier for precise positioning [28].

In addition, related to modeling approach applications of compliant positioners for precise positioning systems [29–31], Hua et al. employed a compliance matrix method to model the quality response of the proposed XYθ positioner [32]. Yang et al. applied Castigliano's second theorem and a beam-constrained model for modeling the static–dynamic characteristics of the developed XY positioner [33]. Moreover, Wang et al. applied compliant matrix method for modeling the output response of the new XY positioner based on the compliant springs [34]. In addition, a 3-dof mechanism was analyzed via a pseudo-rigid-body model (PRBM) [35]. Yang et al. applied the PRBM, Lagrange technique, and GA algorithm for static–dynamic analysis, as well as optimization of main design variables, to enhance the output response of the developed 02-dof platform [24]. In addition, Wu et al. employed a pseudo-rigid body model (PRBM) according to the diagram method for the kinematics and dynamics modeling of the suggested structure [22]. Therefore, based on the advantages of analytic approaches, a hybrid approach combining the PRBM, Lagrange technique, FEA, and Firefly algorithm was proposed in this research for evaluating, validating, and optimizing the output response of the developed fine compliant Z-positioner.

In addition, related to the development of compliant positioners for nanoindentation testers [36], Rabe et al. developed a new compliant platform with an indenter output displacement of 20 µm, combined into an in situ nanoscratch instrument for evaluating the characteristics of the specimen [37]. Huang et al. developed a compact nanoindentation device with an indenter output displacement of 12.8 µm, suitable for potential applications

in in situ nanoindentation of biological specimens, which can be integrated with SEM and transmission electron microscope (TEM) devices [38]. In addition, Huang et al. developed a new fine-compliant positioner integrated with a compliant half-bridge amplifier, achieving a maximized output displacement of 11.44 μm for a novel in situ nanoindentation device [39].

Although numerous compliant mechanisms with one degree of freedom have been developed, there has been little attention devoted to creating a compliant fine Z-positioner integrated with a new hybrid displacement amplifier featuring a symmetric four-lever mechanism and a Scott Russell mechanism for use in an in situ nanoindentation device. Furthermore, there is a need to develop a compliant fine Z-positioner that considers multiple functions simultaneously. To fill the gaps in the literature, the motivation of this paper is to design a novel compliant fine Z-positioner following a symmetric four-lever mechanism, a symmetric Scott Russell mechanism, and a symmetric two-rectangular-hinge-based parallel guiding mechanism for directing the indenter in nanoindentation testing positioning systems.

The novel design of the recent exploration is expressed as follows:

— A new hybrid compliant displacement amplifier, comprising symmetric four-lever and symmetric Scott Russell structures, was integrated into the Z-positioner to enhance the output working stroke for directing the indenter in a nanoindentation testing device;
— A parallel-symmetric leading structure was applied to reduce the small decoupling mobility error according to the symmetrical mechanism to enhance the positioning control;
— A hybrid approach of the PRBM, the Lagrange technique, the Firefly algorithm and FEA analysis was applied for analytical modeling, optimization and result verification.

This paper presents new contributions by design modeling and optimizing an innovative fine Z-positioner for directing the indenter in a nanoindentation testing device. The output response of the fine Z-positioner was initially modeled using the PRBM and the Lagrange technique. Furthermore, the precision of the analytical modeling of the quality responses was validated by finite element analysis. Thirdly, the Firefly algorithm was employed for optimizing the essential design variables of the developed fine Z-platform, based on the sequence of analytical equations [40]. The prototype was ultimately manufactured to validate the best FEA analysis. The input and output displacements were examined to validate the linear correlation between the optimized FEA results and the experimental outcomes for input and output displacement values. According to the FEA and experiment outcomes, the displacement intensification ratios were 6.8725 and 8, respectively. Furthermore, the experiment outcomes revealed a strong linear link between leading mechanisms in nanoindentation positioning systems.

2. Mechanical Structure of a New Flexure-Based 1-DOF Positioner

In this paper, a novel compliant fine Z-positioner is designed for promising use in a nanoindentation assessing system, as revealed in Figure 1. Specifically, the rough Z-positioner is exploited for guiding the bio-sample towards the indenter. The fine Z-platform is then exploited to drive the indenter and examine the bio-specimen's mechanical properties.

In this research, the hybrid displacement amplifier, which combines the eight-lever symmetric mechanism and the Scott Russell mechanism, was integrated into the proposed positioner to enhance the operating travel of the guiding mechanism during the nanoindentation-assessing process. More specifically, the operating principle of a lever structure is illustrated in Figure 2. The input displacement (H_1) is applied at point P, and P′ is achieved H_1 from P in the Y-direction. Meanwhile, point Q′ achieved H_2 from Q in the

Y-direction, as well as the lever rotating around the point O an angle θ. Parameters d_1 and d_2 are dimensions of the PQ lever lengths revolving an O center.

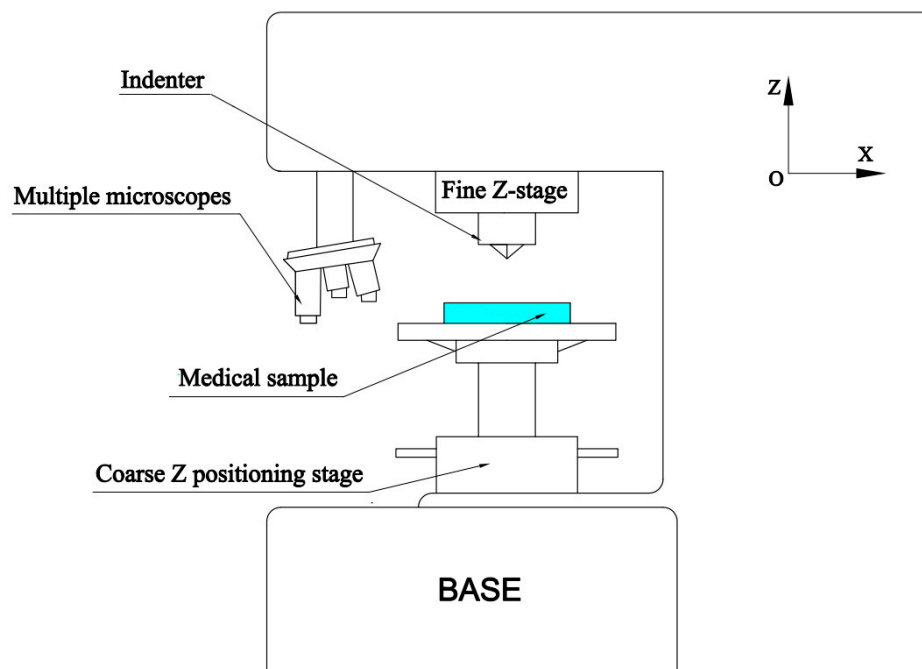$$r_l = \frac{H_2}{H_1} = \frac{d_2}{d_1} \tag{1}$$

Figure 1. A diagram of the proposed bio-specimen testing system.
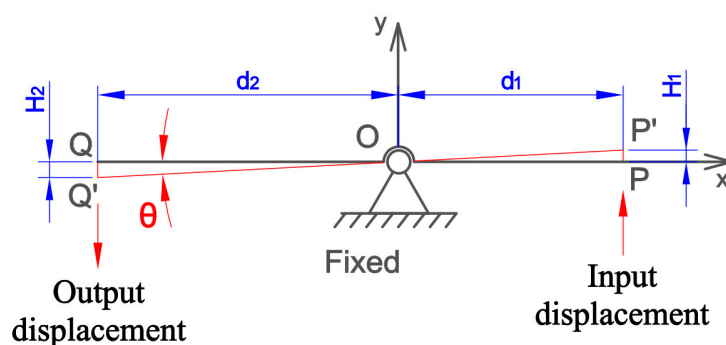

Figure 2. Operation principle of lever structure.

A Scott Russell mechanism was integrated into the hybrid displacement amplifier to increase the operating stroke of the developed positioner. The operation principle of the Scott Russell amplifier was illustrated in Figure 3a,b. As demonstrated in Figure 3, based on the operation rule of the Scott Russell mechanism, the amplification displacement proportion is roughly achieved:

$$r_S = \frac{V_D}{V_A} = \frac{OA}{OD} \tag{2}$$

In addition, to enhance output displacement, a new symmetric hybrid displacement amplifier utilizing an eight-lever mechanism and a Scott Russell mechanism was developed to integrate into the proposed positioner, as shown in Figure 4.
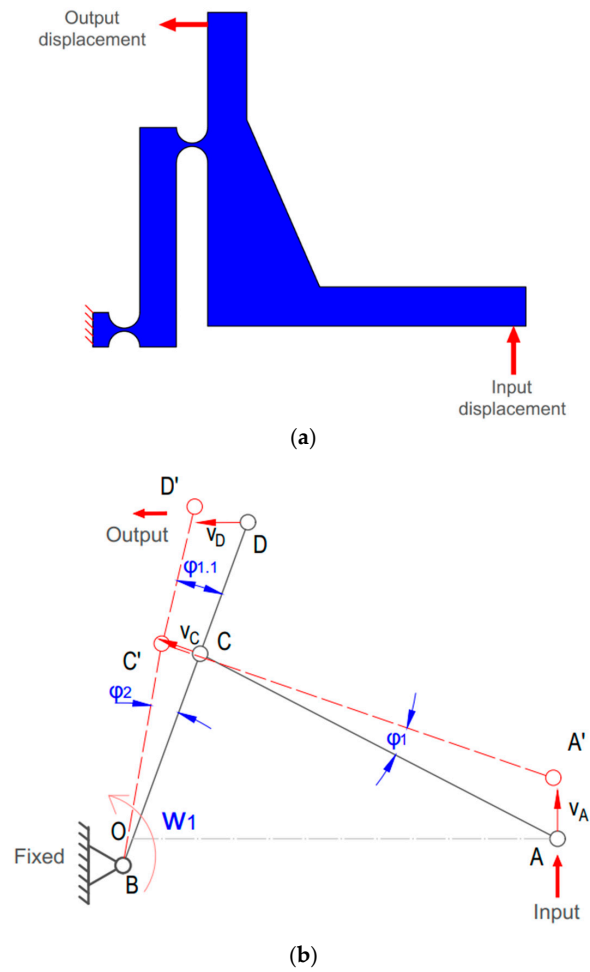
(**a**)

(**b**)

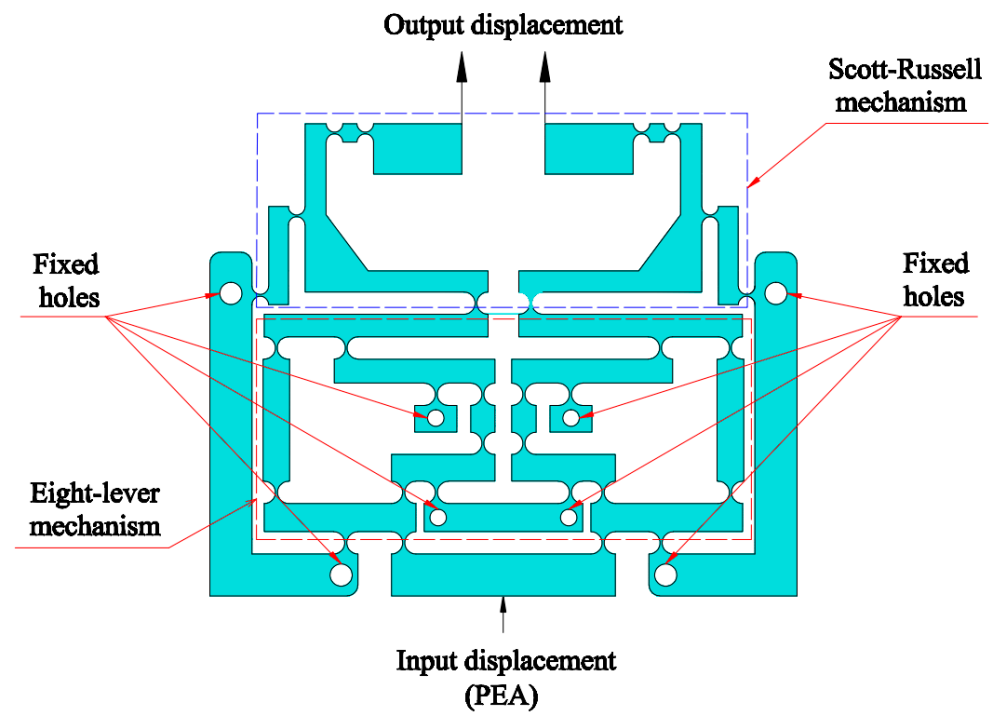**Figure 3.** Diagram: (**a**) Scott Russell amplifier, (**b**) operation principle.

Figure 4. A hybrid symmetric displacement amplifier of four-lever mechanism and Scott Russell mechanism.

In addition, the hybrid amplifier connected with symmetric-parallel leading structure integrated into four rectangular joints to reduce the parasitic motion error as well as keep high output displacement, as demonstrated in Figure 5. More specifically, as depicted in Figure 5, the symmetric four-lever displacement amplifier had symmetric four-floors to reduce a decoupling motion error and ensure a high displacement amplification ratio. Therefore, controlling the number of floors in the multi-lever amplifier-integrated Scott Russell mechanism will provide a high intensification proportion, allowing for efficient observation of the indentation testing procedure. The input displacement is operated by a piezoelectric actuator (PEA). The 3D design model of the advanced Z-stage is revealed in Figure 6.
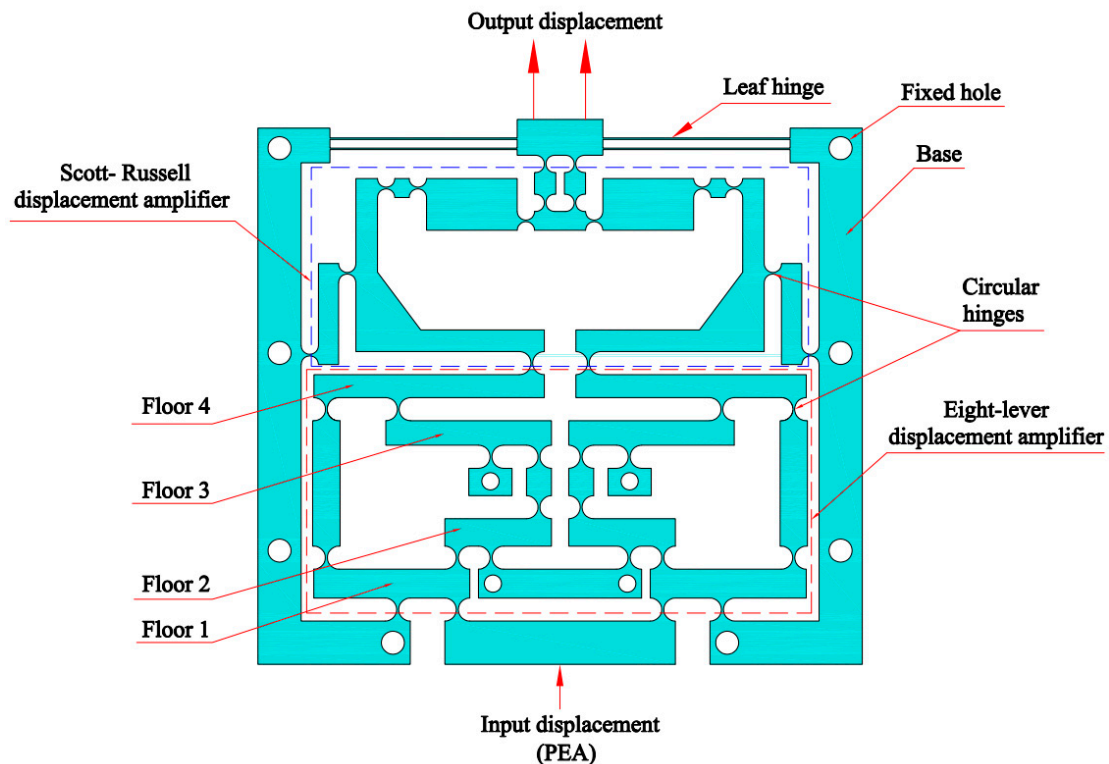

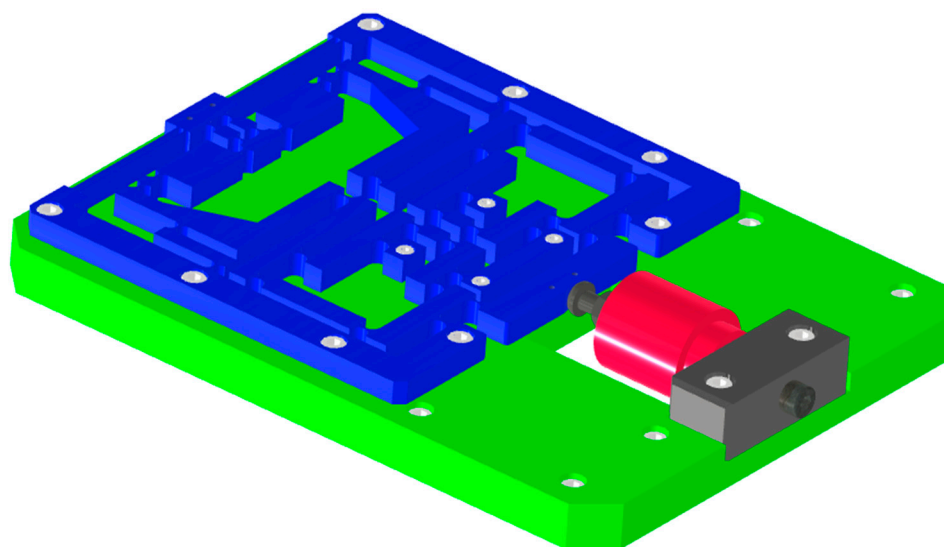**Figure 5.** Structure of proposed complaint 1-DOF positioner.

Figure 6. The assembly cluster 3D design model.

The developed positioner was fabricated from material Al-7075 due to its favourable characteristics, including a high yield strength of 503 MPa, an elastic modulus of 71.7 GPa, and a 2810 kg/m³ density. As illustrated in Figure 7, the total dimensions of the proposed positioner are 210 mm × 186 mm × 10 mm. The positioner included the following parts: (i) a PEA actuator, (ii) a hybrid symmetric displacement amplifier of an eight-lever mechanism and Scott Russell mechanism integrated right circular joints, (iii) a parallel guiding mechanism integrated rectangular joints, and (iv) fixed holes. More specifically, the right circular hinges were selected for the proposed positioner to achieve the desired controlling position accuracy due to their excellent characteristic of high rotary center accuracy [41]. The dimensional schema in Figure 7 illustrates the main dimensional parameters of the proposed positioner, which are used to build an initial design. Additionally, the main dimension values of the proposed positioner are presented in Table 1. More specifically, T_1, T_2, T_3, and T_4 are right circular hinge thicknesses on different floors of the proposed stage with various colors and different values for ensuring the energy transferring efficiency in the diagram, as illustrated in Figure 7. Moreover, D and Y are the lever distances in a lever amplification mechanism.
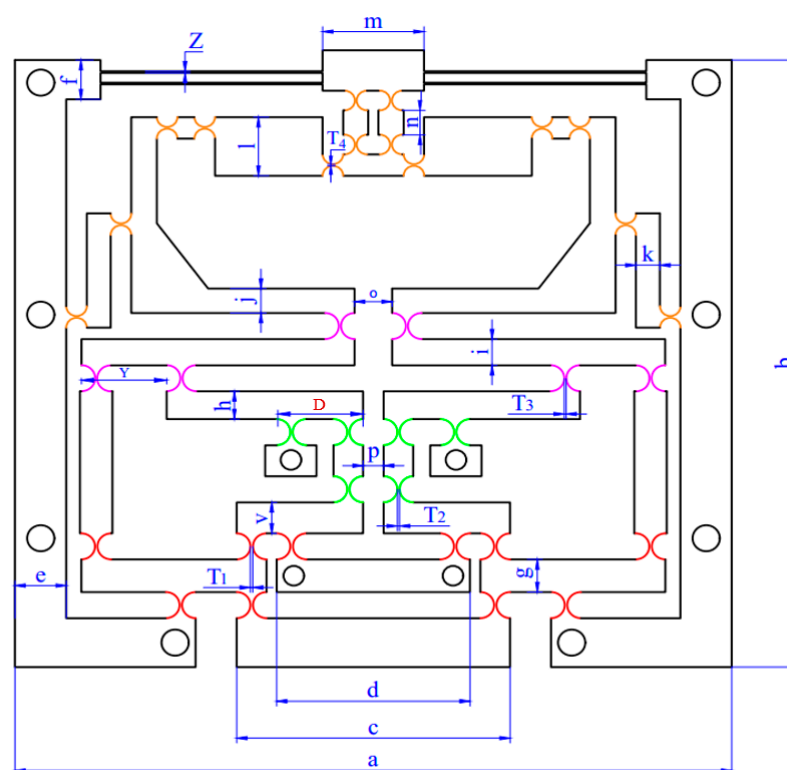

Figure 7. Dimension diagram of the developed fine Z-positioner.

Table 1. Dimension parameters of the developed Z-positioner (unit: mm).

Parameter	Value	Parameter	Value
v	9.5	a	210
g	10	b	186
h	8.5	c	80
i	8	d	56.6
j	7.5	e	15.25
o	11	f	12
k	7	T_1	$1.1 \leq T_1 \leq 1.2$
l	18	T_2	$1 \leq T_2 \leq 1.1$
m	30	T_3	$0.9 \leq T_3 \leq 1$
n	7.5	T_4	$0.8 \leq T_4 \leq 0.9$
p	6	X	$23 \leq D \leq 27$
Z	0.5	Y	$22 \leq Y \leq 26$

3. Analytical Model for Proposed Positioner

3.1. Static–Dynamic Analysis

Firstly, the 3D model of the developed compliant Z-positioner was designed using Inventor Professional software 2024. Second, the static–dynamic characteristics were established using the PRBM and Lagrange technique to evaluate the initial response quickly. Finally, the analytical result was validated by FEA analysis. The PRBM diagram is illustrated in Figure 8. The velocity analysis diagram of the Scott Russell mechanism is also depicted in Figure 9.
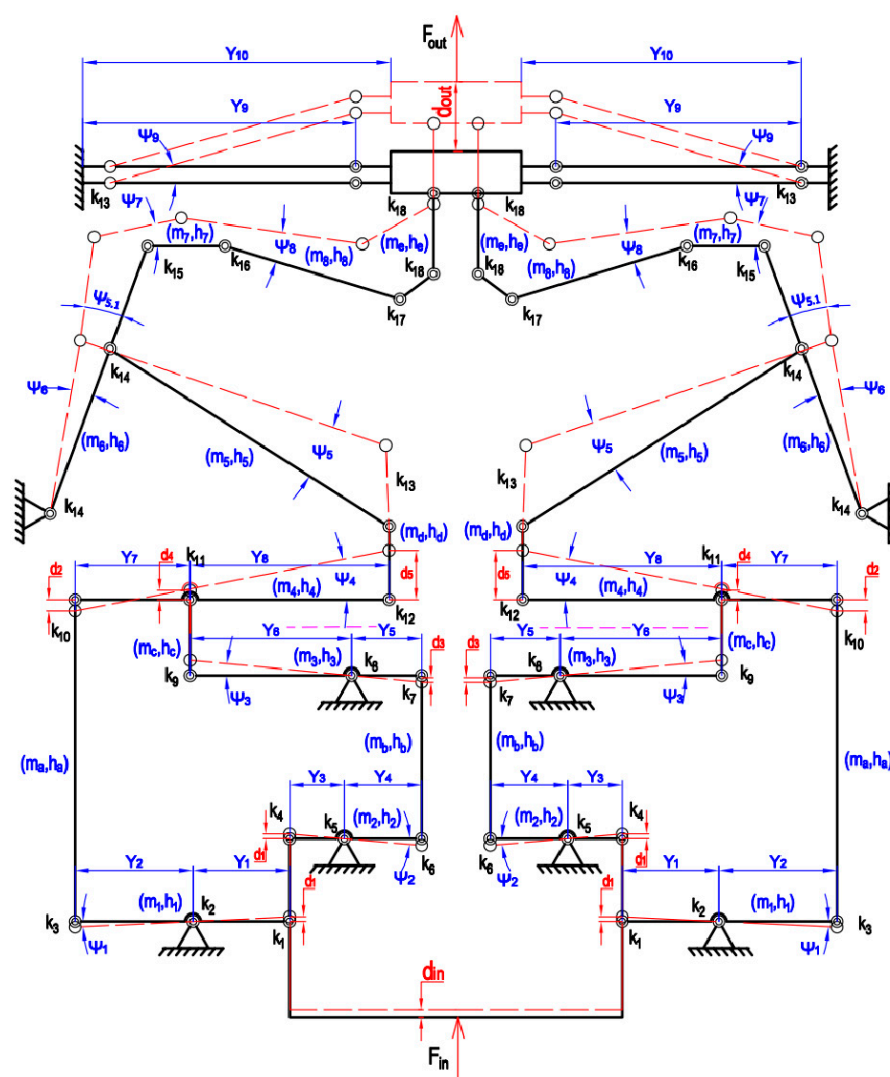

Figure 8. A PRBM diagram for the proposed positioner.

In this research, right circular hinges and rectangular hinges were proposed to integrate into the proposed positioner. More specifically, the right circular hinges were utilized in the hybrid displacement amplifier to achieve a high working stroke and high control motion accuracy. Additionally, rectangular hinges were used for the parallel guiding mechanism to achieve a tiny decoupling mobility error and a high output displacement. The significant factors of the two flexure-based hinges were illustrated in Figures 10 and 11. More specifically, r_c, w_c, and t_c, as depicted in Figure 10, are the key parameters of the right circular joint, representing the radius, width, and thickness, respectively. In addition, l_r and b_r, as demonstrated in Figure 11, are the key parameters of the rectangular hinge, corresponding to the length and width, respectively.

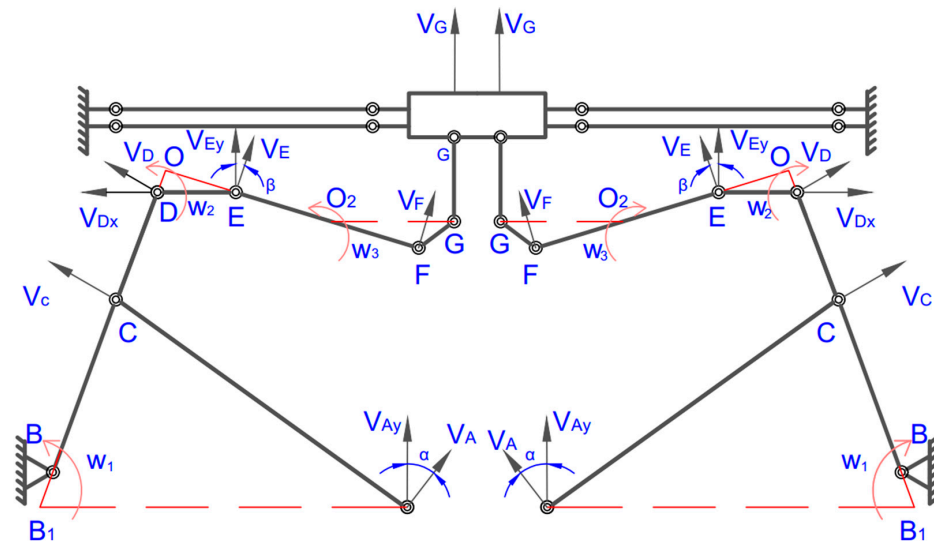**Figure 9.** Velocity analysis diagram based on the PRBM for the proposed positioner.
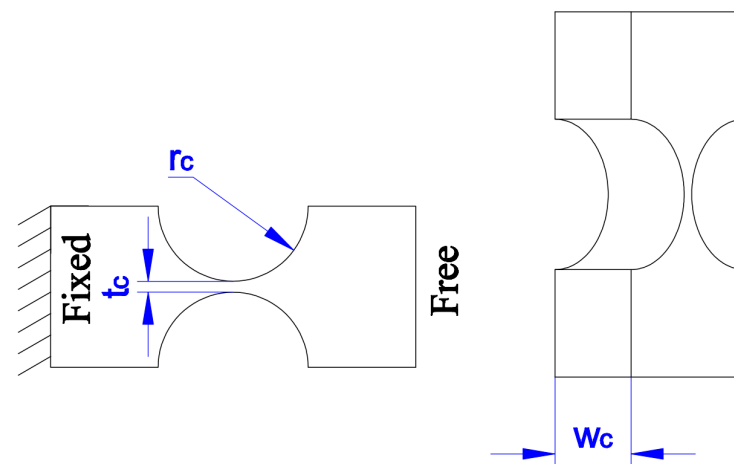

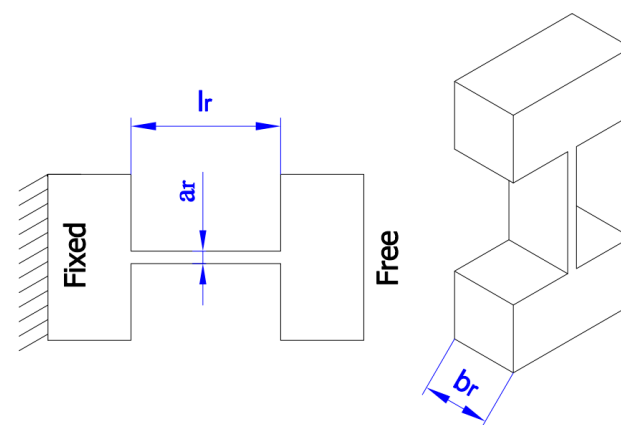**Figure 10.** Key factors of a compliant right circular hinge.

Figure 11. Key factors of a compliant rectangular hinge.

As demonstrated in Figures 10 and 11, a chain of analytical equations for calculating the displacement amplification ratio is the following Equations (3)–(15):

$$d_2 = \frac{d_1 \times Y_2}{Y_1} \tag{3}$$

$$d_3 = \frac{d_1 \times Y_4}{Y_3} \tag{4}$$

$$d_4 = \frac{d_3 \times Y_6}{Y_5} = d_1 \frac{Y_4 \times Y_6}{Y_3 \times Y_5} \tag{5}$$

$$d_5 = \frac{d_4 \times (Y_7 + Y_8)}{Y_7} + d_2 \frac{Y_8}{Y_7} = d_1 \left(\frac{Y_4 \times Y_6 \times (Y_7 + Y_8)}{Y_3 \times Y_5 \times Y_7} + \frac{Y_2 \times Y_8}{Y_1 \times Y_7} \right) \tag{6}$$

$$v_{Ay} = w_1 \times Y_{B1d} \tag{7}$$

$$v_A = \frac{v_{Ay}}{\cos(\alpha)} \tag{8}$$

$$v_C = w_1 \times Y_{B1C} \tag{9}$$

$$v_D = w_1 \times Y_{B1D} = w_2 \times Y_{OD} \tag{10}$$

$$v_{Ey} = v_E \times \cos(\beta) \tag{11}$$

$$v_E = w_2 \times Y_{OE} = w_3 \times Y_{O2E} \tag{12}$$

$$v_F = w_3 \times Y_{O2F} \tag{13}$$

$$v_G = w_3 \times Y_{O2G} = v_{Ay} \left(\frac{Y_{B1D} \times Y_{O2G} \times Y_{OE}}{Y_{B1A} \times Y_{OD} \times Y_{O2E}} \right) \tag{14}$$

$$AR = \left(\frac{Y_{B1D} \times Y_{O2G} \times Y_{OE}}{Y_{B1A} \times Y_{OD} \times Y_{O2E}} \right) \times \left(\frac{Y_4 \times Y_6 \times (Y_7 + Y_8)}{Y_3 \times Y_5 \times Y_7} + \frac{Y_2 \times Y_8}{Y_1 \times Y_7} \right) \tag{15}$$

where m_i symbolizes the mass, Y_i ($i = 1, 2 \ldots 9, 10$) is the length, and $\Psi_j (j = 1, 2 \ldots 8, 9)$ denotes the rotating angles of the stiff hinges.

The torsional stiffness (K_C) of the right circular hinge, the torsional stiffness (K_L) of the rectangular hinge, and the harsh linkage inertia moment (I_C) are illustrated in Equations (16)–(18).

$$K_c = \frac{2 \times E \times b_c \times t_c^{2.5}}{9 \times \pi \times r_c^{0.5}} \tag{16}$$

$$K_L = \frac{E \times a_r^3 \times b_r}{12 \times l} \tag{17}$$

$$I_C = \frac{m \times Y_j^2}{12} \tag{18}$$

In Figures 8 and 9, the kinetic energy of the developed positioner is identified as the following equation:

$$E_{KT} = \sum_1^9 (E_t + E_r) = \sum_1^9 \left(\frac{1}{2} m_i v_i^2 + \frac{1}{2} I_i \dot{\Psi}_j^2 \right) \Psi \tag{19}$$

Employing Equation (19), the kinetic energy of every rigid linkage is computed by the following equation:

$$
\begin{aligned}
E_{KT} = {} & \tfrac{1}{2} m_1 \times \left(\tfrac{Y_1 + Y_2}{2} \dot{\Psi}_1 \right)^2 + \tfrac{1}{2} I_1 \times \left(\dot{\Psi}_1 \right)^2 + \tfrac{1}{2} m_2 \times \left(\tfrac{Y_3 + Y_4}{2} \dot{\Psi}_2 \right)^2 + \tfrac{1}{2} I_2 \times \left(\dot{\Psi}_2 \right)^2 \\
& + \tfrac{1}{2} m_a \times \left(\tfrac{Y_1 + Y_2}{2} \dot{\Psi}_1 \right)^2 + \tfrac{1}{2} m_3 \times \left(\tfrac{Y_5 + Y_6}{2} \dot{\Psi}_3 \right)^2 + \tfrac{1}{2} I_3 \times \left(\dot{\Psi}_3 \right)^2 + \tfrac{1}{2} m_b \times \left(\left(\tfrac{Y_3 + Y_4}{2} \right) \dot{\Psi}_2 \right)^2 \\
& + \tfrac{1}{2} m_c \times \left(\left(\tfrac{Y_5 + Y_6}{2} \right) \dot{\Psi}_3 \right)^2 + \tfrac{1}{2} m_4 \times \left(\tfrac{Y_7 + Y_8}{2} \dot{\Psi}_4 \right)^2 + \tfrac{1}{2} I_4 \times \left(\dot{\Psi}_4 \right)^2 + \tfrac{1}{2} m_d \times \left((Y_7 + Y_8) \dot{\Psi}_4 \right)^2 \\
& + \tfrac{1}{2} m_5 \times \left(Y_{CA} \times \dot{\Psi}_5 \right)^2 + \tfrac{1}{2} m_5 \times \left(Y_{CD} \times \dot{\Psi}_{5.1} \right)^2 + \tfrac{1}{2} I_5 \times \left(\dot{\Psi}_5 \right)^2 + \tfrac{1}{2} I_{5\_1} \times \left(\dot{\Psi}_{5\_1} \right)^2 \\
& + \tfrac{1}{2} m_6 \times \left(Y_{BC} \times \dot{\Psi}_6 \right)^2 + \tfrac{1}{2} I_6 \times \left(\dot{\Psi}_6 \right)^2 + \tfrac{1}{2} m_7 \times \left(Y_{DE} \times \dot{\Psi}_7 \right)^2 + \tfrac{1}{2} I_7 \times \left(\dot{\Psi}_7 \right)^2 \\
& + \tfrac{1}{2} m_8 \times \left(Y_{EF} \times \dot{\Psi}_8 \right)^2 + \tfrac{1}{2} I_8 \times \left(\dot{\Psi}_8 \right)^2 + \tfrac{1}{2} m_e \times \left(Y_{EG} \times \dot{\Psi}_8 \right)^2 \\
& + \tfrac{1}{2} m_9 \times \left(\tfrac{Y_9}{2} \times \dot{\Psi}_9 \right)^2 + \tfrac{1}{2} I_9 \times \left(\dot{\Psi}_9 \right)^2
\end{aligned} \tag{20}
$$

The elastic energy of the developed positioner is identified as:

$$E_{VT} = \sum_{J=1}^{9} \frac{1}{2} K_j \Psi_j{}^2 \tag{21}$$

The elastic energy is derived from the deformation of both flexure-based right circular joints and rectangular joints.

$$E_{VT} = \frac{1}{2}(k_1 + k_2 + k_3)(\Psi_1)^2 + \frac{1}{2}(k_4 + k_5 + k_6)(\Psi_2)^2 + \frac{1}{2}(k_7 + k_8 + k_9)(\Psi_3)^2 + \frac{1}{2}(k_{10} + k_{11} + k_{12})(\Psi_4)^2$$

$$+ \frac{1}{2}(k_{13})(\Psi_5)^2 + \frac{1}{2}(k_{15})(\Psi_5)^2 + \frac{1}{2}(k_{14})(\Psi_6)^2 + \frac{1}{2}(k_{16})(\Psi_7)^2 + \frac{1}{2}(k_{17} + 2k_{18})(\Psi_8)^2 + \frac{1}{2}(4k_{19})(\Psi_9)^2 \tag{22}$$

The rotary angle and angle speed of every linkage are symbolized. The connections among the rotational angles are established by:

$$\Psi_1 = \frac{d_1}{Y_1} \tag{23}$$

$$\Psi_2 = \Psi_1 \times \frac{Y_1}{Y_3} \tag{24}$$

$$\Psi_3 = \Psi_1 \times \frac{Y_1 \times Y_4 \times Y_6}{Y_3 \times Y_5{}^2} \tag{25}$$

$$\Psi_4 = \Psi_1 \times \left(\frac{Y_1 \times Y_4 \times Y_6}{Y_3 \times Y_5 \times Y_7} + \frac{Y_2 \times Y_8}{(Y_7 + Y_8) \times Y_7} \right) \tag{26}$$

$$\Psi_5 = \Psi_1 \left(\frac{Y_1 \times Y_4 \times Y_6 \times (Y_7 + Y_8)}{Y_3 \times Y_5 \times Y_7 \times Y_{AC} \times \cos\alpha} + \frac{Y_2 \times Y_8}{Y_7 \times Y_{AC} \times \cos\alpha} \right) \tag{27}$$

$$\Psi_{5.1} = \Psi_1 \times Y_{B1D} \times \frac{(Y_1 \times Y_4 \times Y_6 \times (Y_7 + Y_8)) + (Y_2 \times Y_8 \times Y_3 \times Y_5)}{Y_3 \times Y_5 \times Y_7 \times Y_{CD} \times Y_{B1A}} \tag{28}$$

$$\Psi_6 = \Psi_1 \times Y_{B1C} \times \left(\frac{Y_1 \times Y_4 \times Y_6 \times (Y_7 + Y_8)}{Y_3 \times Y_5 \times Y_7 \times Y_{B1A} \times Y_{BC}} + \frac{Y_2 \times Y_8}{Y_7 \times Y_{B1A} \times Y_{BC}} \right) \tag{29}$$

$$\Psi_7 = \Psi_1 \times Y_{B1D} \times Y_{OE} \times \cos(\beta) \times \frac{(Y_1 \times Y_4 \times Y_6 \times (Y_7 + Y_8)) + (Y_2 \times Y_8 \times Y_3 \times Y_5)}{Y_3 \times Y_5 \times Y_7 \times Y_{DE} \times Y_{B1A} \times Y_{OD}} \tag{30}$$

$$\Psi_8 = \Psi_1 \times Y_{B1D} \times Y_{OE} \times Y_{O2F} \times \frac{(Y_1 \times Y_4 \times Y_6 \times (Y_7 + Y_8)) + (Y_2 \times Y_8 \times Y_3 \times Y_5)}{Y_3 \times Y_5 \times Y_7 \times Y_{B1A} \times Y_{OD} \times Y_{O2E} \times Y_{EF}} \tag{31}$$

$$\Psi_9 = \Psi_1 \times Y_{B1D} \times Y_{OE} \times Y_{O2G} \times \frac{(Y_1 \times Y_4 \times Y_6 \times (Y_7 + Y_8)) + (Y_2 \times Y_8 \times Y_3 \times Y_5)}{Y_3 \times Y_5 \times Y_7 \times Y_{B1A} \times Y_{OD} \times Y_{O2E} \times Y_9} \tag{32}$$

Using an input force F_{in}, the work is identified by the subsequent equation:

$$W = \frac{1}{2} F_{in} \times d_{in} \tag{33}$$

Given $W = E_V$, the relationships of input force as well as input displacement are established by the subsequent equation:

$$\frac{1}{2}F_{in} \times \mathrm{d}_{in} = \frac{1}{2}\begin{bmatrix} (k_1 + k_2 + k_3)\frac{1}{Y_1} + (k_4 + k_5 + k_6)\left(\frac{1}{Y_3}\right)^2 + (k_7 + k_8 + k_9)\left(\frac{Y_4 \times Y_6}{Y_3 \times Y_5{}^2}\right)^2 \\[2mm] +(k_{10} + k_{11} + k_{12})\left(\frac{Y_4 \times Y_6}{Y_3 \times Y_5 \times Y_7} + \frac{Y_2 \times Y_8}{(Y_7 + Y_8) \times Y_7 \times Y_1}\right)^2 \\[2mm] +(k_{13})\left(\frac{Y_4 \times Y_6 \times (Y_7 + Y_8)}{Y_3 \times Y_5 \times Y_7 \times Y_{AC} \times \cos a} + \frac{Y_2 \times Y_8}{Y_1 \times Y_7 \times Y_{AC} \times \cos a}\right)^2 \\[2mm] +(k_{15})\left(Y_{B1D} \times \frac{(Y_4 \times Y_6 \times (Y_7 + Y_8)) + (Y_2 \times Y_8 \times Y_3 \times Y_5)}{Y_3 \times Y_5 \times Y_7 \times Y_{CD} \times Y_{B1A}}\right)^2 \\[2mm] +(2 \times k_{14})\left(Y_{B1C} \times \left(\frac{Y_4 \times Y_6 \times (Y_7 + Y_8)}{Y_3 \times Y_5 \times Y_7 \times Y_{B1A} \times Y_{BC}} + \frac{Y_2 \times Y_8}{Y_1 \times Y_7 \times Y_{B1A} \times Y_{BC}}\right)\right)^2 \\[2mm] +(k_{16})\left(Y_{B1D} \times Y_{OE} \times \cos(\beta) \times \frac{(Y_4 \times Y_6 \times (Y_7 + Y_8)) + (Y_2 \times Y_8 \times Y_3 \times Y_5)}{Y_3 \times Y_5 \times Y_7 \times Y_{DE} \times Y_{B1A} \times Y_{OD}}\right)^2 \\[2mm] +(k_{17} + 2k_{18})\left(Y_{B1D} \times Y_{OE} \times Y_{O2F} \times \frac{(Y_4 \times Y_6 \times (Y_7 + Y_8)) + (Y_2 \times Y_8 \times Y_3 \times Y_5)}{Y_3 \times Y_5 \times Y_7 \times Y_{B1A} \times Y_{OD} \times Y_{O2E} \times Y_{EF}}\right)^2 \\[2mm] +(2k_{19})\left(Y_{B1D} \times Y_{OE} \times Y_{O2G} \times \frac{(Y_4 \times Y_6 \times (Y_7 + Y_8)) + (Y_2 \times Y_8 \times Y_3 \times Y_5)}{Y_3 \times Y_5 \times Y_7 \times Y_{B1A} \times Y_{OD} \times Y_{O2E} \times Y_9}\right)^2 \end{bmatrix} d_{in}{}^2 \tag{34}$$

Based on Equation (34), dividing by two aspects, the stiffness is determined via the subsequent equation:

$$k_{in} = (k_1 + k_2 + k_3)\frac{1}{Y_1} + (k_4 + k_5 + k_6)\left(\frac{1}{Y_3}\right)^2 + (k_7 + k_8 + k_9)\left(\frac{Y_4 \times Y_6}{Y_3 \times Y_5{}^2}\right)^2$$

$$+(k_{10} + k_{11} + k_{12})\left(\frac{Y_4 \times Y_6}{Y_3 \times Y_5 \times Y_7} + \frac{Y_2 \times Y_8}{(Y_7 + Y_8) \times Y_7 \times Y_1}\right)^2$$

$$+(k_{13})\left(\frac{Y_4 \times Y_6 \times (Y_7 + Y_8)}{Y_3 \times Y_5 \times Y_7 \times Y_{AC} \times \cos \alpha} + \frac{Y_2 \times Y_8}{Y_1 \times Y_7 \times Y_{AC} \times \cos \alpha}\right)^2$$

$$+(k_{15})\left(Y_{B1D} \times \frac{(Y_4 \times Y_6 \times (Y_7 + Y_8)) + (Y_2 \times Y_8 \times Y_3 \times Y_5)}{Y_3 \times Y_5 \times Y_7 \times Y_{CD} \times Y_{B1A}}\right)^2 \tag{35}$$

$$+(2 \times k_{14})\left(Y_{B1C} \times \left(\frac{Y_4 \times Y_6 \times (Y_7 + Y_8)}{Y_3 \times Y_5 \times Y_7 \times Y_{B1A} \times Y_{BC}} + \frac{Y_2 \times Y_8}{Y_1 \times Y_7 \times Y_{B1A} \times Y_{BC}}\right)\right)^2$$

$$+(k_{16})\left(Y_{B1D} \times Y_{OE} \times \cos(\beta) \times \frac{(Y_4 \times Y_6 \times (Y_7 + Y_8)) + (Y_2 \times Y_8 \times Y_3 \times Y_5)}{Y_3 \times Y_5 \times Y_7 \times Y_{DE} \times Y_{B1A} \times Y_{OD}}\right)^2$$

$$+(k_{17} + 2k_{18})\left(Y_{B1D} \times Y_{OE} \times Y_{O2F} \times \frac{(Y_4 \times Y_6 \times (Y_7 + Y_8)) + (Y_2 \times Y_8 \times Y_3 \times Y_5)}{Y_3 \times Y_5 \times Y_7 \times Y_{B1A} \times Y_{OD} \times Y_{O2E} \times Y_{EF}}\right)^2$$

$$+(2k_{19})\left(Y_{B1D} \times Y_{OE} \times Y_{O2G} \times \frac{(Y_4 \times Y_6 \times (Y_7 + Y_8)) + (Y_2 \times Y_8 \times Y_3 \times Y_5)}{Y_3 \times Y_5 \times Y_7 \times Y_{B1A} \times Y_{OD} \times Y_{O2E} \times Y_9}\right)^2$$

The mobility formulation is identified by the subsequent equation:

$$\overline{M}\ddot{\Psi}_1 + \overline{K}\Psi_1 = 0 \tag{36}$$

$$\overline{M} = m_1 \times \left(\frac{Y_1+Y_2}{2}\right)^2 + I_1 + m_2 \times \left(\frac{Y_1\times(Y_3+Y_4)}{2\times Y_3}\right)^2 + I_2 \times \left(\frac{Y_1}{Y_3}\right)^2 + m_a \times \left(\frac{Y_1+Y_2}{2}\right)^2$$

$$+ m_3 \times \left(\frac{(Y_5+Y_6)\times Y_1\times Y_4\times Y_6}{2\times Y_3\times Y_5{}^2}\right)^2 + I_3 \times \left(\frac{Y_1\times Y_4\times Y_6}{Y_3\times Y_5{}^2}\right)^2 + m_b \times \left(\frac{Y_1\times(Y_3+Y_4)}{2\times Y_3}\right)^2$$

$$+ m_c \times \left(\frac{(Y_5+Y_6)\times Y_1\times Y_4\times Y_6}{2\times Y_3\times Y_5{}^2}\right)^2 + m_4 \times \left(\frac{Y_7+Y_8}{2} \times \left(\frac{Y_1\times Y_4\times Y_6}{Y_3\times Y_5\times Y_7} + \frac{Y_2\times Y_8}{(Y_7+Y_8)\times Y_7}\right)\right)^2$$

$$+ I_4 \times \left(\left(\frac{Y_1\times Y_4\times Y_6}{Y_3\times Y_5\times Y_7} + \frac{Y_2\times Y_8}{(Y_7+Y_8)\times Y_7}\right)\right)^2 + m_d \times \left((Y_7+Y_8)\left(\frac{Y_1\times Y_4\times Y_6}{Y_3\times Y_5\times Y_7} + \frac{Y_2\times Y_8}{(Y_7+Y_8)\times Y_7}\right)\right)^2$$

$$+ m_5 \times \left(l_{CA} \times \frac{Y_1\times Y_4\times Y_6\times(Y_7+Y_8)}{Y_3\times Y_5\times Y_7\times l_{AC}\times\cos a} + \frac{Y_2\times Y_8}{Y_7\times l_{AC}\times\cos a}\right)^2$$

$$+ m_5 \times l_{B1D} \times \frac{(Y_1\times Y_4\times Y_6\times(Y_7+Y_8))+(Y_2\times Y_8\times Y_3\times Y_5)}{Y_3\times Y_5\times Y_7\times l_{CD}\times l_{B1A}}$$

$$+ I_5 \times \left(\frac{Y_1\times Y_4\times Y_6\times(Y_7+Y_8)}{Y_3\times Y_5\times Y_7\times l_{AC}\times\cos a} + \frac{Y_2\times Y_8}{Y_7\times l_{AC}\times\cos a}\right)^2$$

$$+ I_{5.1} \times \left(l_{B1D} \times \frac{(Y_1\times Y_4\times Y_6\times(Y_7+Y_8))+(Y_2\times Y_8\times Y_3\times Y_5)}{Y_3\times Y_5\times H_7\times l_{CD}\times l_{B1A}}\right)$$

$$+ m_6 \times \left(l_{BC} \times l_{B1C} \times \left(\frac{Y_1\times Y_4\times Y_6\times(Y_7+Y_8)}{Y_3\times Y_5\times Y_7\times l_{B1A}\times l_{BC}} + \frac{Y_2\times Y_8}{Y_7\times l_{B1A}\times l_{BC}}\right)\right)^2 \tag{37}$$

$$+ I_6 \times \left(l_{B1C} \times \left(\frac{Y_1\times Y_4\times Y_6\times(Y_7+Y_8)}{Y_3\times Y_5\times Y_7\times l_{B1A}\times l_{BC}} + \frac{Y_2\times Y_8}{Y_7\times l_{B1A}\times l_{BC}}\right)\right)^2$$

$$+ m_7 \times \left(l_{DE} \times l_{B1D} \times l_{OE} \times \cos(\beta) \times \frac{(Y_1\times Y_4\times Y_6\times(Y_7+Y_8))+(Y_2\times Y_8\times Y_3\times Y_5)}{Y_3\times Y_5\times Y_7\times l_{DE}\times l_{B1A}\times l_{OD}}\right)^2$$

$$+ I_7 \times \left(l_{B1D} \times l_{OE} \times \cos(\beta) \times \frac{(Y_1\times Y_4\times Y_6\times(Y_7+Y_8))+(Y_2\times Y_8\times Y_3\times Y_5)}{Y_3\times Y_5\times Y_7\times l_{DE}\times l_{B1A}\times l_{OD}}\right)^2$$

$$+ m_8 \times \left(l_{EF} \times l_{B1D} \times l_{OE} \times l_{O2F} \times \frac{(Y_1\times Y_4\times Y_6\times(Y_7+Y_8))+(Y_2\times Y_8\times Y_3\times Y_5)}{Y_3\times Y_5\times Y_7\times l_{B1A}\times l_{OD}\times l_{O2E}\times l_{EF}}\right)^2$$

$$+ I_8 \times \left(l_{B1D} \times l_{OE} \times l_{O2F} \times \frac{(Y_1\times Y_4\times Y_6\times(Y_7+Y_8))+(Y_2\times Y_8\times Y_3\times Y_5)}{Y_3\times Y_5\times Y_7\times l_{B1A}\times l_{OD}\times l_{O2E}\times l_{EF}}\right)^2$$

$$+ m_e \times \left(l_{EG} \times l_{B1D} \times l_{OE} \times l_{O2F} \times \frac{(Y_1\times Y_4\times Y_6\times(Y_7+Y_8))+(Y_2\times Y_8\times Y_3\times Y_5)}{Y_3\times Y_5\times Y_7\times l_{B1A}\times l_{OD}\times l_{O2E}\times l_{EF}}\right)^2$$

$$+ m_9 \times \left(Y_9 \times l_{B1D} \times l_{OE} \times l_{O2G} \times \frac{(Y_1\times Y_4\times Y_6\times(Y_7+Y_8))+(Y_2\times Y_8\times Y_3\times Y_5)}{Y_3\times Y_5\times Y_7\times l_{B1A}\times l_{OD}\times l_{O2E}\times Y_9}\right)^2$$

$$+ I_9 \times \left(Y_9 \times l_{B1D} \times l_{OE} \times l_{O2G} \times \frac{(Y_1\times Y_4\times Y_6\times(Y_7+Y_8))+(Y_2\times Y_8\times Y_3\times Y_5)}{Y_3\times Y_5\times Y_7\times l_{B1A}\times l_{OD}\times l_{O2E}\times Y_9}\right)^2$$

$$\overline{K} = (k_1 + k_2 + k_3) + (k_4 + k_5 + k_6)\left(\frac{Y_1}{Y_3}\right)^2 + (k_7 + k_8 + k_9)\left(\frac{Y_1 \times Y_4 \times Y_6}{Y_3 \times Y_5{}^2}\right)^2$$

$$+ (k_{10} + k_{11} + k_{12})\left(\frac{Y_1 \times Y_4 \times Y_6}{Y_3 \times Y_5 \times Y_7} + \frac{Y_2 \times Y_8}{(Y_7 + Y_8) \times Y_7}\right)^2$$

$$+ (k_{13})\left(\frac{Y_1 \times Y_4 \times Y_6 \times (Y_7 + Y_8)}{Y_3 \times Y_5 \times Y_7 \times l_{AC} \times \cos a} + \frac{Y_2 \times Y_8}{Y_7 \times l_{AC} \times \cos a}\right)^2$$

$$+ (k15)\left(l_{B1D} \times \frac{(Y_1 \times Y_4 \times Y_6 \times (Y_7 + Y_8)) + (Y_2 \times Y_8 \times Y_3 \times Y_5)}{Y_3 \times Y_5 \times H_7 \times l_{CD} \times l_{B1A}}\right)^2$$

$$+ (2 \times k14)\left(l_{B1C} \times \left(\frac{Y_1 \times Y_4 \times Y_6 \times (Y_7 + Y_8)}{Y_3 \times Y_5 \times Y_7 \times l_{B1A} \times l_{BC}} + \frac{Y_2 \times Y_8}{Y_7 \times l_{B1A} \times l_{BC}}\right)\right)^2 \qquad (38)$$

$$+ (k_{16})\left(l_{B1D} \times l_{OE} \times \cos(\beta) \times \frac{(Y_1 \times Y_4 \times Y_6 \times (Y_7 + Y_8)) + (Y_2 \times Y_8 \times Y_3 \times Y_5)}{Y_3 \times Y_5 \times Y_7 \times l_{DE} \times l_{B1A} \times l_{OD}}\right)^2$$

$$+ (k_{17} + 2k_{18})\left(l_{B1D} \times l_{OE} \times l_{O2F} \times \frac{(Y_1 \times Y_4 \times Y_6 \times (Y_7 + Y_8)) + (Y_2 \times Y_8 \times Y_3 \times Y_5)}{Y_3 \times Y_5 \times Y_7 \times l_{B1A} \times l_{OD} \times l_{O2E} \times l_{EF}}\right)^2$$

$$+ (2k_{19})\left(l_{B1D} \times l_{OE} \times l_{O2G} \times \frac{(Y_1 \times Y_4 \times Y_6 \times (Y_7 + Y_8)) + (Y_2 \times Y_8 \times Y_3 \times Y_5)}{Y_3 \times Y_5 \times Y_7 \times l_{B1A} \times l_{OD} \times l_{O2E} \times Y_9}\right)^2$$

The developed fine Z-positioner's initial resonant frequency (unit: Hz) is identified as the following equation:

$$f = \frac{1}{2\pi} \times \sqrt{\frac{1000 \times \overline{k}}{\overline{M}}} \qquad (39)$$

3.2. Analytic Model Validation

The Skewness standard was used in this study to determine the meshing feature. The findings revealed that the medium worth of this standard was around 0.55, as shown in Figure 12. Therefore, the achieved value guarantees an appropriate mesh for the developed positioner in the simulated process by FEA analysis.
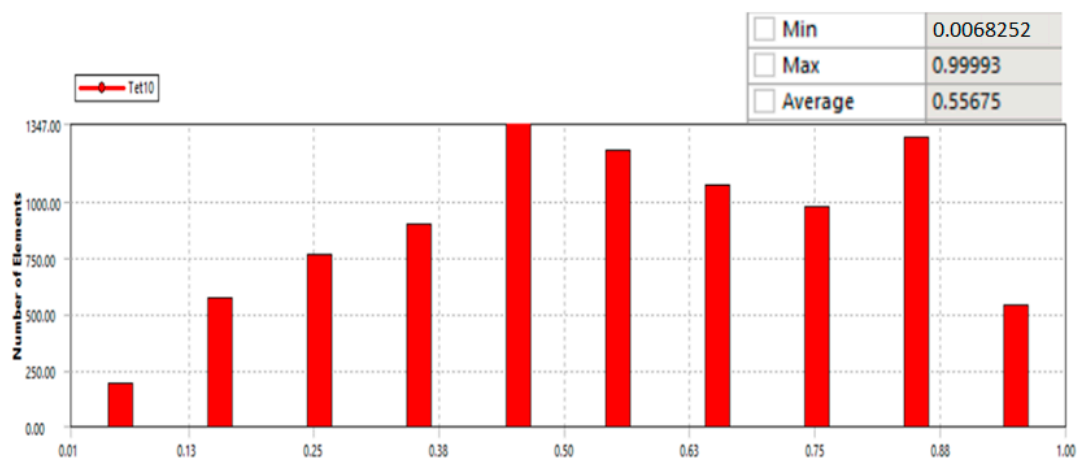

Figure 12. Diagram for evaluating the mesh feature based on the Skewness standard.

The analytical outcomes are corroborated using FEM. The analytical approach yielded a natural frequency of 171.746 Hz. Still, the first natural frequency derived from the FEA data was 172.76 Hz, as illustrated in Figure 13. The inaccuracy between the theoretical value and the FEA assessment, as presented in Table 2, is approximately 0.5869%. The devised

analytical approach is reliable and effective for assessing the fundamental attributes of the proposed positioner.
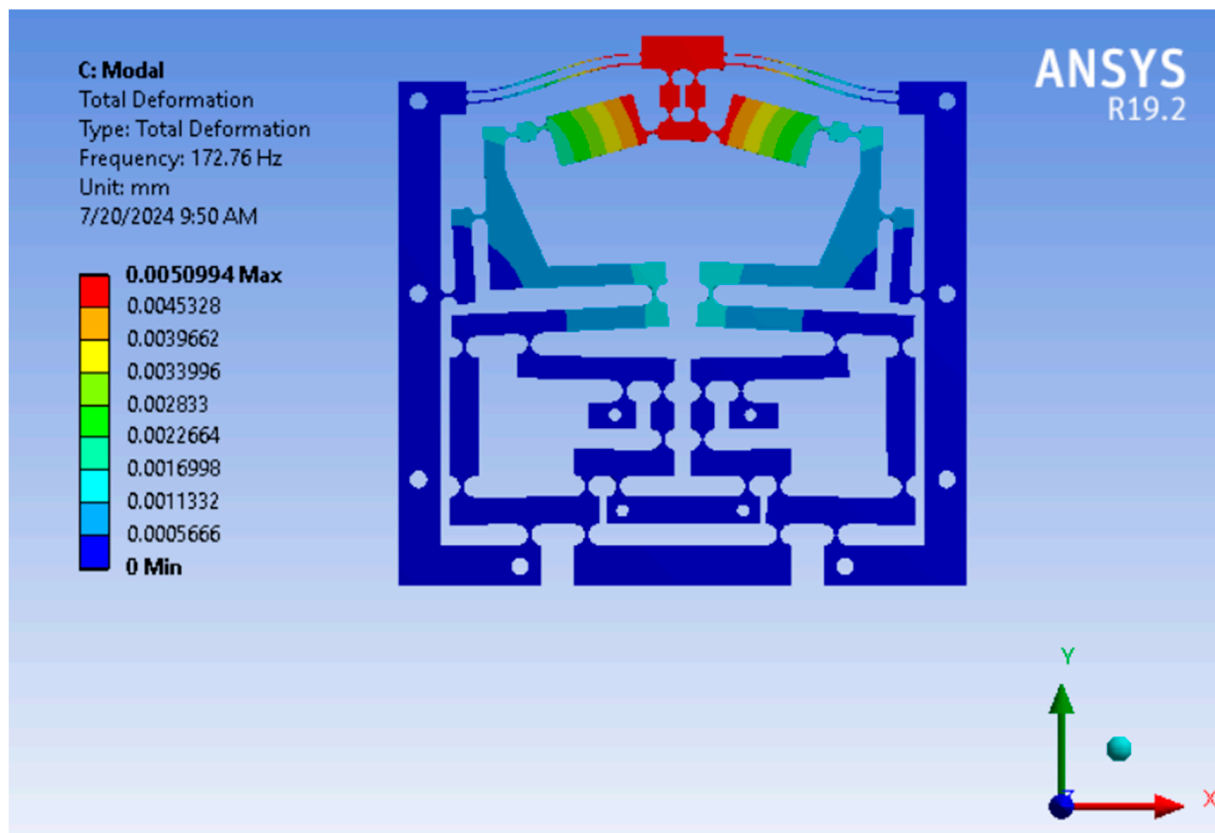

Figure 13. The first natural frequency of the initial design based on FEA analysis.

Table 2. Verification of the analytical result by FEA analysis for the initial design.

Attribute	Analytic Outcome	FEA Outcome	Inaccuracy
f (Hz)	171.746	172.76	0.5869%

3.3. Decoupling Mobility Error Analysis for Developed Positioner

As the developed Z-platform moved in the Z-direction, a comparable movement in the X-direction was also detected. A parasitic motion inaccuracy is the unwanted motion in the X-direction. Based on the FEA outcomes, the decoupling movement imprecision was negligible, calculated to be only 0.095% (below 0.1%), as shown in Table 3. Therefore, the decoupling movement imprecision has little effect on output deformation accurateness. The advanced Z-mechanism exhibits a good linear relationship between input and output displacements, causing it well-suited for exact localization and nanoindentation checking devices. The Equation for calculating the decoupling mobility error is expressed as follows:

$$e = \frac{z}{y} \times 100\% \tag{40}$$

The signs, including e, z, and y, are the decoupling mobility imprecision, Z-axis output displacement, and output X-axis displacement, respectively.

Table 3. FEA results of input–output displacements and parasitic motion inaccuracy (unit: μm).

No.	Input Displacement	Output Displacement (Z-Direction)	Output Displacement (X-Direction)	Parasitic Motion Inaccuracy (%)
1	2	13.6281	0.013	0.09539114
2	4	27.2562	0.0261	0.09562795
3	6	40.8843	0.0391	0.09562832
4	8	54.5125	0.0521	0.09562795
5	10	68.1406	0.0652	0.09562714
6	12	81.7687	0.0782	0.09562832
7	14	95.3968	0.0912	0.09562819
8	16	109.0249	0.1043	0.09562795
9	18	122.6530	0.1173	0.09562701
10	20	136.2811	0.1303	0.09562714
11	22	149.9093	0.1434	0.09562801
12	24	163.5374	0.1564	0.09562832
13	26	177.1655	0.1694	0.09562789
14	28	190.7936	0.1825	0.09562819
15	30	204.4217	0.1955	0.09562781
16	32	218.0498	0.2085	0.09562795
17	34	231.6779	0.2215	0.09562765
18	36	245.3061	0.2346	0.09562701
19	38	258.9342	0.2476	0.09562813
20	40	272.5623	0.2606	0.09562714
21	42	286.1904	0.2737	0.09562819
22	44	299.8185	0.2867	0.09562801
23	46	313.4466	0.2997	0.09562754
24	48	327.0747	0.3128	0.09562832
25	50	340.7029	0.3258	0.09562764
26	52	354.3310	0.3388	0.09562789
27	54	367.9591	0.3519	0.09562823
28	56	381.5872	0.3649	0.09562819
29	58	395.2153	0.3779	0.09562815
30	60	408.8434	0.3910	0.09562781

4. Suggested Hybrid Approach

The design of the new positioner is based on a hybrid symmetric amplifier of the eight-lever mechanism, the Scott Russell mechanism, and a parallel mechanism for guiding the nanoindentation testing process. Firstly, the static–dynamic attributes of the proposed positioner were established using the pseudo-rigid-body methodology and the Lagrange technique to promptly evaluate the output response of the advanced Z-platform. Secondly, analytical models were verified by FEA analysis. Thirdly, according to mathematical equations, the Firely algorithm was used to optimize main design variables for enhancing the output attribute. Finally, the prototype was fabricated to verify the FEA result. More details about the conceptual framework flowchart of the proposed hybrid approach were demonstrated in Figure 14.

- Develop a novel structure for potential application in guiding mechanisms for nanoindentation testing systems, utilizing a new hybrid displacement magnifier and a symmetric-parallel leading structure.
- Establish static and dynamic characteristics by the PRBM and Lagrange technique.
- Validate analytical results by FEA analysis.
- Define the main input parameters, output response, as well as limits and constraints for design variables and objective function.
- Optimize main design variables to enhance the quality response using the algorithm.
- Verify optimized results by FEA analysis.
- Fabricate the prototype based on optimal results.
- Conduct experiments to check the quality response and validate FEA results.
- Compare the quality response of the proposed positioner with the prior research.
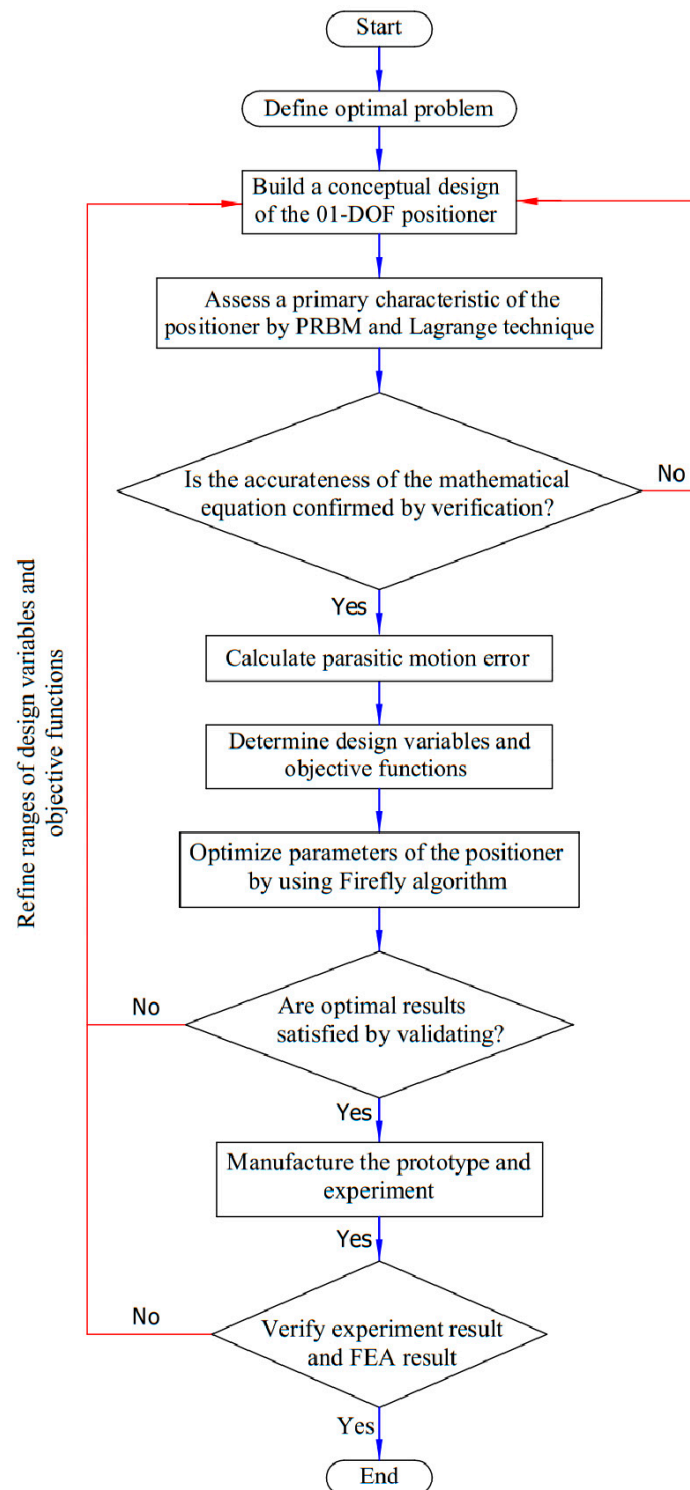
Figure 14. Conceptual framework flowchart of the proposed hybrid approach for the proposed positioner.

4.1. Parameter Optimization of a Fine Z-Positioner

The developed compliant structure operates based on the elastic deformation of the flexure hinges; the resonant frequency is as high as feasible to enhance the responsiveness of the developed Z-platform. Thus, the initial natural frequency should be optimized to improve response speed and mitigate resonance. This article addresses an optimization problem focused on maximizing the resonant frequency, which is succinctly stated as follows:

Search for main parameter vector: $X = [t_1, t_2, t_3, t_4, t_5, t_6]$

$$\text{Maximize } f(X) \tag{41}$$

$$\text{Restriction: } f(X) > 100 \text{ (Hz)} \tag{42}$$

Constrictions of main parameters:

$$
\begin{aligned}
1.1 &\le T_1 \le 1.2 \\
1 &\le T_2 \le 1.1 \\
0.9 &\le T_3 \le 1 \\
0.8 &\le T_4 \le 0.9 \\
23 &\le D \le 27 \\
22 &\le Y \le 26
\end{aligned} \tag{43}
$$

in which $f(X)$ denotes the resonant frequency, t_1, t_2, t_3, t_4, t_5, and t_6 are T_1, T_2, T_3, T_4, D and Y, respectively, as depicted in Figure 7. More specifically, T_1, T_2, T_3, T_4 are the various flexure hinge thicknesses at four lever floors with four colours including red, green, pink and orange, respectively. In addition, D and Y are distances between the two flexure hinge centres on the third and fourth floors.

The spectrum of design factors is contingent upon design experiences and the attributes of various floors to ensure adequate transmission energy. The thickness of the 1st floor must exceed that of the second storey. The thickness of the 2nd floor must exceed that of the 3rd floor. This is essential to augment the robustness of the suggested stage and minimize the dissipation of displacement energy. Simultaneously, the optimization procedure should determine an adequate thickness for various locations across several floors to identify the most suitable values for the proposed construction.

The incorporation method of the PRBM, the Lagrange technique, and the Firefly algorithm was developed using MATLAB 2021, as outlined in a series of Equations (1)–(39) and (41)–(43). The optimized design variables of the developed Z-platform were acquired as follows: $T_1 = 0.75$ mm, $T_2 = 0.7$ mm, $T_3 = 0.65$ mm, $T_4 = 0.6$ mm, $D = 27$ mm, and $Y = 26$ mm. The optimized outcome indicates that the optimized resonant frequency based on the analytical approach is approximately 220.16 Hz. Figure 15 illustrates the convergence behavior of the offered approach.
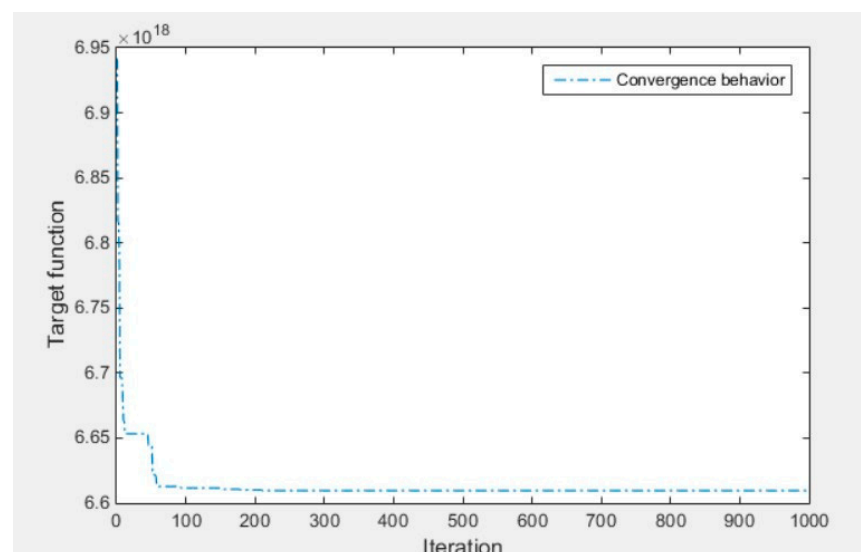

Figure 15. Proposed algorithm convergence diagram.

4.2. FEA Verification

The optimized factors were utilized to create a 3D construction. According to the FEA result, the initial natural frequency is 198.86 Hz. Furthermore, the error between the optimum and FEA results for the 1st resonant frequency was 9.67%, as shown in Table 4. This outcome suggests that the approach framework described is reliable for forming the advanced positioner. Table 5 shows that, in contrast to the initial structure outcome, the frequency of the advanced positioner increased by 13.12%. Additionally, as depicted in Figure 16a–f, the natural frequencies for the six modes are 198.86 Hz, 344.19 Hz, 478.65 Hz, 703.67 Hz, 707.6 Hz, and 711.91 Hz, respectively. As a result, the resonant frequency values listed above, especially the 2nd natural frequency, as illustrated in Figure 16b, should be examined to prevent damage to the suggested positioner.
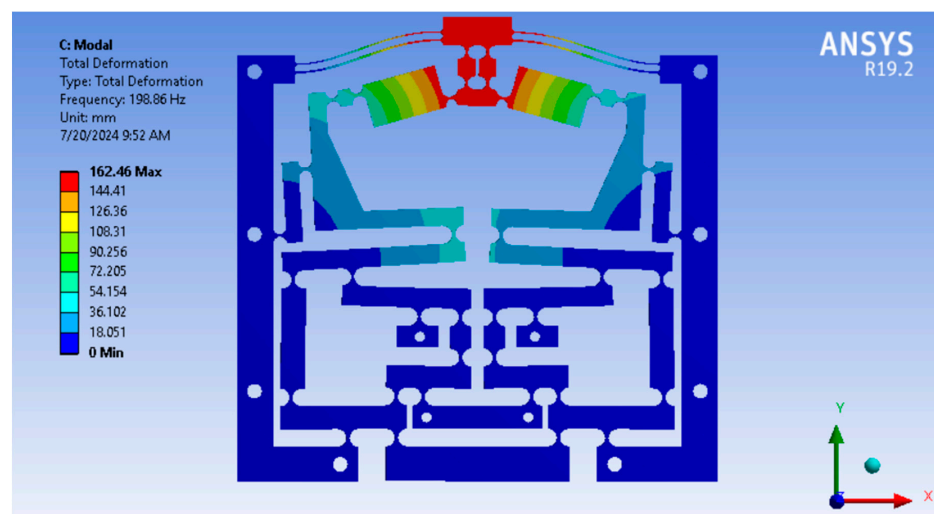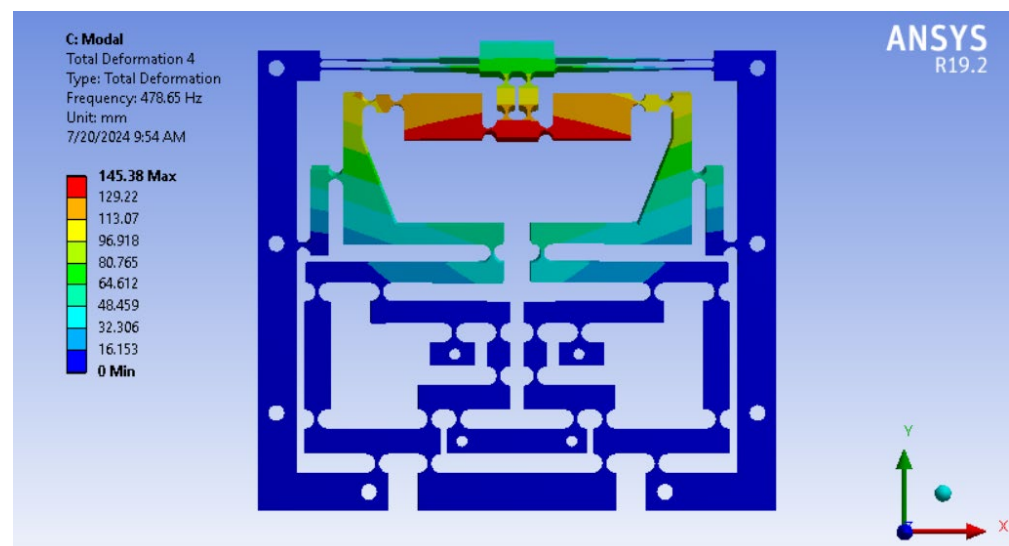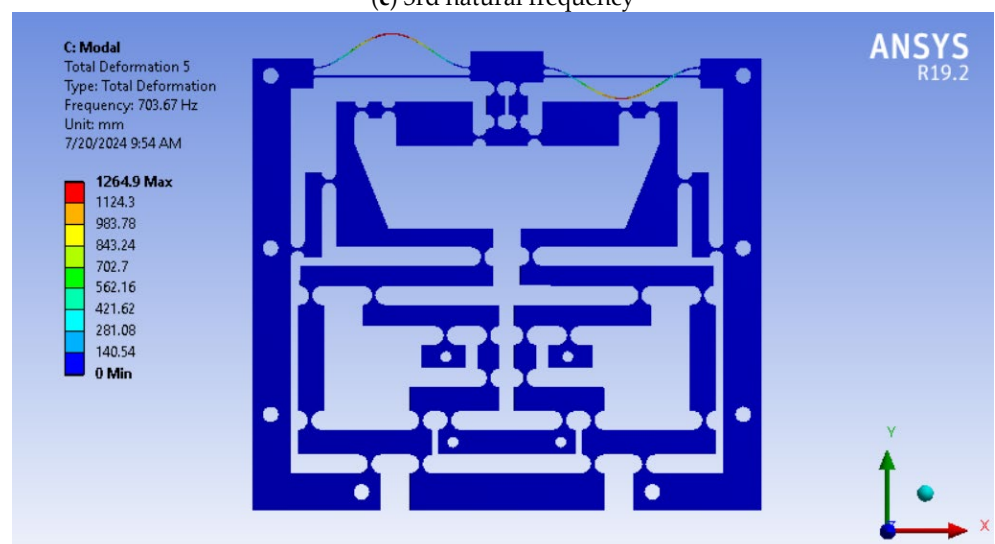

(**a**) 1st natural frequency
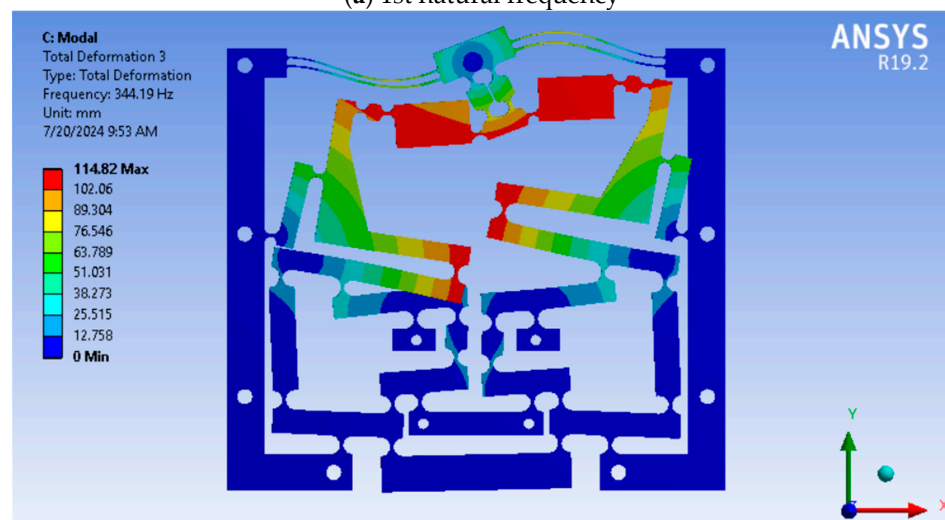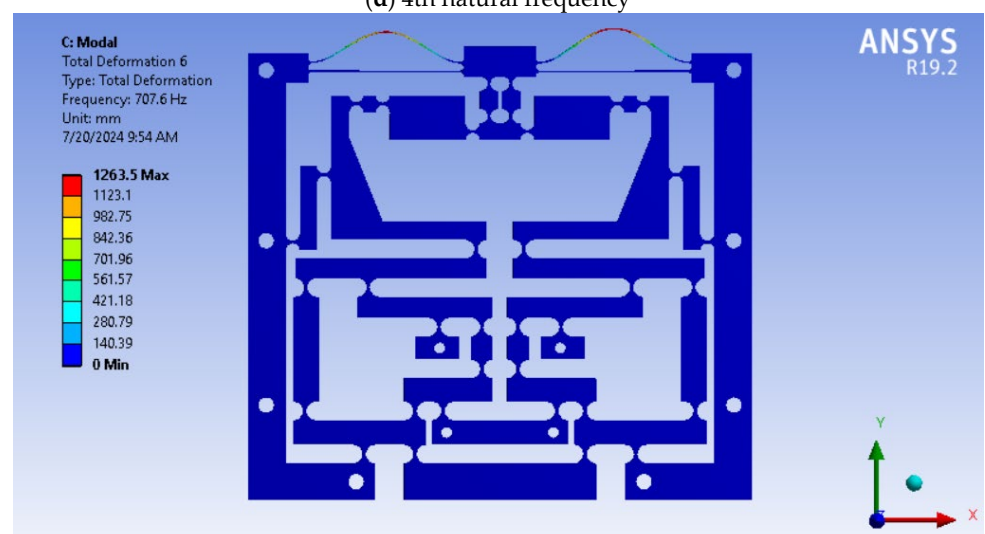

(**b**) 2nd natural frequency

Figure 16. *Cont.*
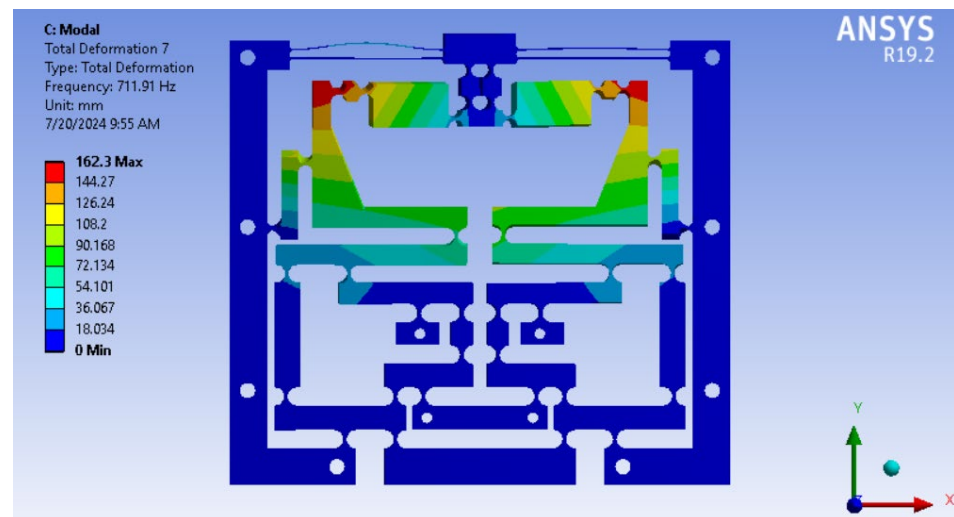
(**c**) 3rd natural frequency

(**d**) 4th natural frequency

(**e**) 5th natural frequency

Figure 16. *Cont*.

(**f**) 6th natural frequency

Figure 16. The frequency results of the optimized stage based on FEA analysis.

Table 4. Verification of the optimized result by FEA.

| Response	Optimized Theory Outcome	FEA Outcome	Imprecision
f (Hz)	220.16	198.86	9.67%

Table 5. Evaluation of the optimization and draft structures.

Attribute	Optimized Structure	Primary Structure	Enhancement
f (Hz)	198.86	172.76	13.12%

4.3. Experiment Investigation

4.3.1. Prototype Production and Experiment Layout

A prototype of the optimized positioner was produced to verify the output characteristic of the suggested structure. This research utilized a computerized numerical control milling technique to manufacture the optimized prototype. Figure 17 illustrates the constructed prototype and device configuration designed for evaluating the output response of the advanced positioner. The compliant positioner was actuated using the PEA (PI 225.10, PI, Karlsruhe, Germany), with a maximal working travel of 15 μm. The input and output displacements were quantified utilizing two laser displacement sensors, which possess a precision of 0.05 μm (LK-G30, Keyence, Osaka, Japan).
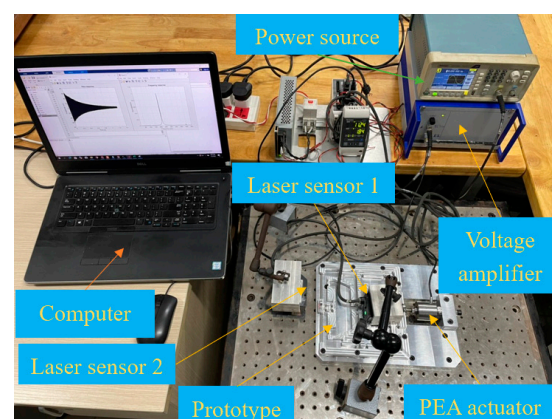
Figure 17. Experiment configuration for determining the resonant frequency.

4.3.2. Experiment Outcomes

The experiment configuration, illustrated in Figure 17, was established to evaluate the initial natural response to the suggested hammer testing methodology. The LK-G30 sensor precisely measured the vibration on the center platform along the Z-axis, achieving a resolution of 0.05 μm. The LK-G30 sensor was utilized in this study to capture signals and record data through control software, as illustrated in Figure 17. The collected data were subsequently evaluated using the rapid Fourier transformation procedure implemented in MATLAB R2021b to ascertain the resonant frequency.

The advanced Z-platform's initial resonant frequency was verified by the FEA frequency result of 198.86 Hz, which was obtained using Ansys software R19.2. The prototype's high-quality surface was achieved by employing computer numerical control milling to manufacture the proposed design. The experimental natural frequency at the initial crest was 223.541 Hz, as illustrated in Figure 18. Table 6 indicates that the experimental findings and finite element analysis had a discrepancy of 11.04%. The obtained inaccuracy suggests that the Z-positioner's measured natural frequency was close to the FEA outcome. The relationship diagram between input and output displacement based on the optimized and experimental results was illustrated in Figure 19. The achieved results were compared with the ref. [42], as illustrated in Table 7. In addition, the output working stroke of the developed Z-positioner was compared with the previous studies, as illustrated in Table 8.
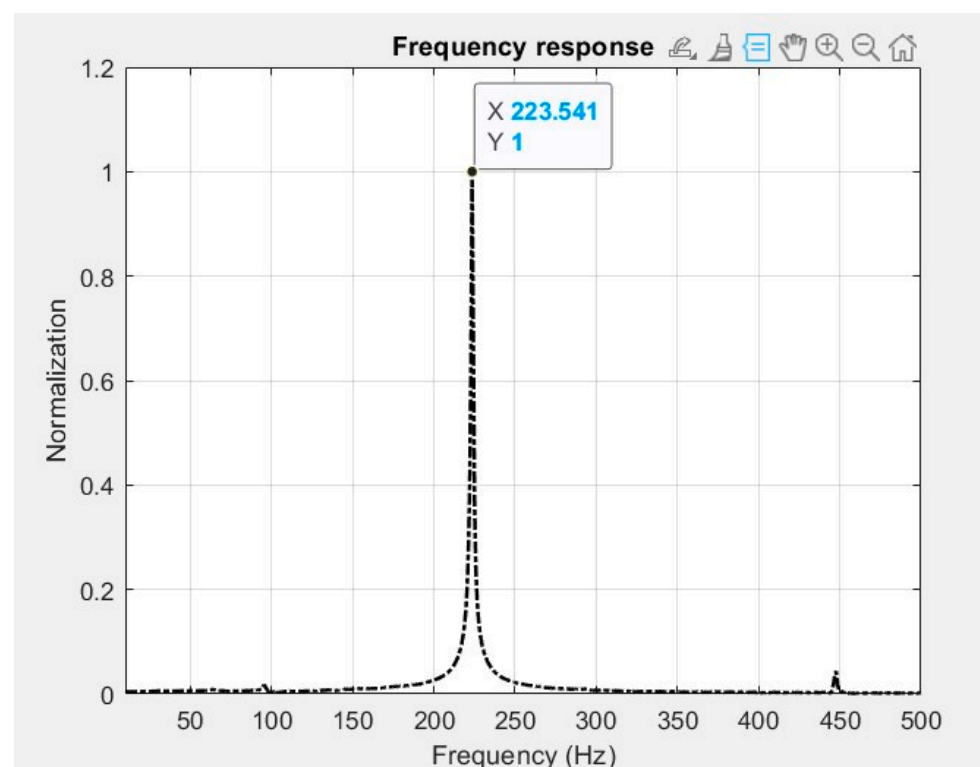

Figure 18. The experiment resonant frequency.

Table 6. Comparison of experiment and FEA outcomes.

Attribute	FEA	Experiment	Inaccuracy
f (Hz)	198.86	223.541	11.04%

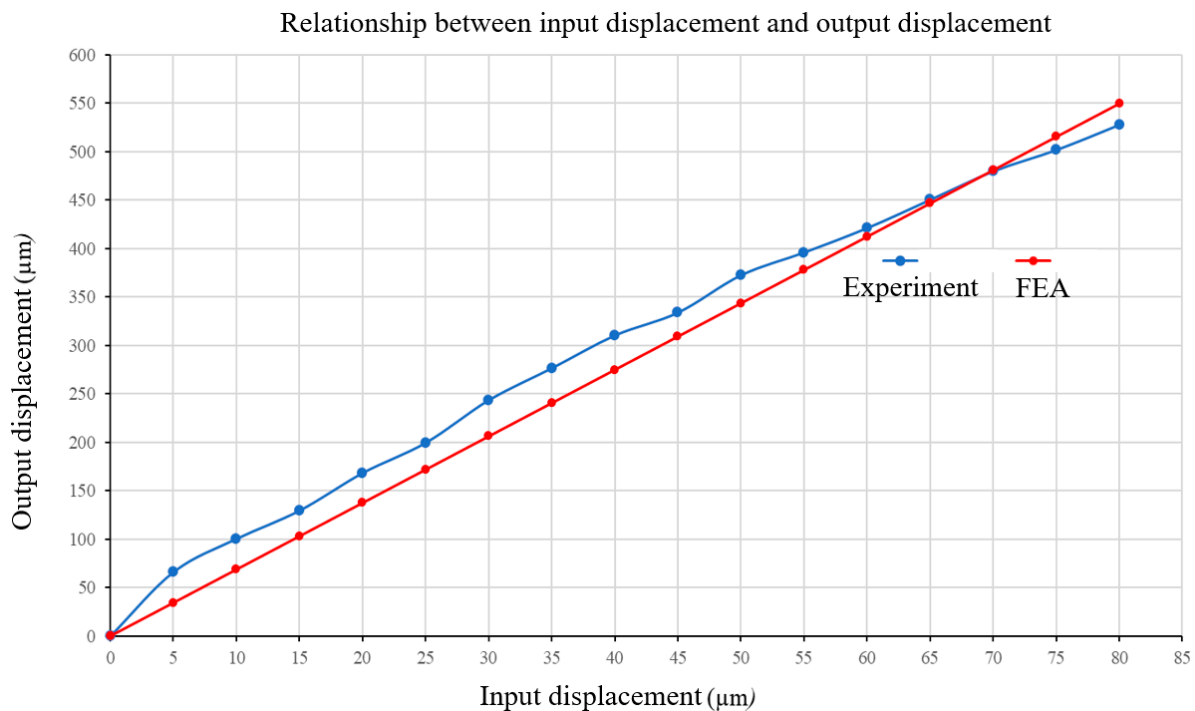## Relationship between input displacement and output displacement

Figure 19. Illustration showing the correlation among the values of displacement measured at the input and output points.

Table 7. Comparison of the achieved results by the present study with those of the previous study.

Attributes	Present Study	Ref. [42]
Amplification ratio (FEA)	6.8725	6.68
Amplification ratio (experiment)	8	6.5
First natural frequency (FEA)	198.86	203.37
First natural frequency (experiment)	223.541	-

Table 8. Comparison of the working stroke by the present study with that of the previous studies.

Study	Total Size	Working Stroke
Present study	210 mm $\times$ 186 mm $\times$ 10 mm	527.6 μm
[39]	103 mm $\times$ 74 mm $\times$ 60 mm	11.4 μm
[37]	-	20 μm

5. Conclusions

This study presents an innovative structure of a compliant fine Z-positioner for guiding the indenter in nanoindentation testing positioning systems. The proposed structure was based on the new hybrid displacement amplifier of the symmetric four-lever mechanism and Scott Russell, and the parallel guiding mechanism integrated into two symmetric rectangular hinges. Next, the static–dynamic characteristic was modeled using the PRBM-Lagrange technique to evaluate the advanced Z-platform's output response quickly. The analytic result was validated by FEA analysis, and the error between the two methods was 0.5869%. According to a chain of analytical equations for calculating the quality response, the Firefly algorithm was executed to determine the optimized design variables, thereby enhancing the output response of the developed positioner.

The optimized design variables were determined as T_1 = 0.75 mm, T_2 = 0.7 mm, T_3 = 0.65 mm, T_4 = 0.6 mm, D = 27 mm, and Y = 26 mm. The optimized resonant frequency derived from the analytical method was around 220.16 Hz. The FEA validation result

indicated that the initial natural frequency was 198.86 Hz. The discrepancy between the optimization and FEA values was 9.67%. The FEA validation produced a result near the optimal outcome of the integration method. Furthermore, the optimization outcome surpassed the initial design.

In addition, the experimental frequency of the proposed positioner was 223.541 Hz. The inaccuracy among the FEA consequences, as well as the experimental consequences, was 11.04%. The connection among the input–output deformations in the Z-direction was also examined. The obtained results demonstrate that the relationship between the input displacement and the output displacement of the experiment and the FEA results of the constructed prototype, exhibits a good linear relationship. Based on the FEA and experiment results, displacement amplification ratios were 6.8725 and 8, respectively. Consequently, the developed structure will be a suitable design for a nanoindentation checking positioning system to assess the mechanical properties of biological specimens.

Future investigations will involve fabricating innovative prototypes with compact structures utilizing additive manufacturing or computerized wire-cutting methods to assess computational outcomes. The current study's limitation is that the proposed Z-positioner's total size was relatively large. Therefore, new designs will be developed with a compact size to be integrated into the scanning electron microscopes (SEM) and other in situ nanoindentation systems in future studies. In addition, a pocket-sized precision positioner will be incorporated into an in situ nanoindentation instrument.

Author Contributions: Conceptualization, M.P.D. and T.D.L.; Methodology, H.G.L. and M.P.D.; Software, M.P.D. and T.D.L.; Validation, M.P.D. and T.D.L.; Formal Analysis, C.T.T. and H.G.L.; Investigation, T.D.L. and C.T.T.; Data Curation, M.P.D.; Writing—original draft preparation, M.P.D.; writing—review and editing, M.P.D. All authors have read and agreed to the published version of the manuscript.

Data Availability Statement: The original contributions presented in the study are included in the article, further inquiries can be directed to the corresponding author.

Conflicts of Interest: The authors declare that they have no known competing financial interests or personal relationships that could have appeared to influence the work reported in this paper.

References

1. Xu, Q. Design and testing of a novel multi-stroke micropositioning system with variable resolutions. *Rev. Sci. Instrum.* **2014**, *85*, 025002. [CrossRef]
2. Gan, J.; Xie, W.; Yang, W.; Lei, S.; Lei, B. Design of a novel Z-shaped flexure hinge and a 2DOF XY precision positioning platform. *Precis. Eng.* **2025**, *93*, 459–469. [CrossRef]
3. Phan, T.V.; Truong, V.M.; Pham, H.T.; Nguyen, V.K. Design of a novel large-stroke compliant constant-torque mechanism based on chained beam-constraint model. *J. Mech. Robot.* **2024**, *16*, 081006-9. [CrossRef]
4. Chen, Q.; Zhang, X.; Zhang, H.; Zhu, B.; Chen, B. Topology optimization of bistable mechanisms with maximized differences between switching forces in forward and backward direction. *Mech. Mach. Theory* **2019**, *139*, 131–143. [CrossRef]
5. Le Chau, N.; Tran, N.T.; Dao, T.P. A multi-response optimal design of bistable compliant mechanism using efficient approach of desirability, fuzzy logic, ANFIS and LAPO algorithm. *Appl. Soft Comput.* **2020**, *94*, 106486. [CrossRef]
6. Gu, Y.; Duan, X.; Lin, J.; Yi, A.; Kang, M.; Jiang, J.; Zhou, W. Design, analysis, and testing of a novel 2-DOF vibration-assisted polishing device driven by the piezoelectric actuators. *Int. J. Adv. Manuf. Technol.* **2020**, *111*, 471–493. [CrossRef]
7. Dang, M.P.; Tran, C.T.; Le, H.G.; Tran, V.Q.A.; Tran, H.V. Modelling and Design Optimization of a Novel Compliant XY Positioner for Vibration-Assisted CNC Milling. *Machines* **2024**, *12*, 534. [CrossRef]
8. Paniselvam, V.; Tan, N.Y.J.; Anantharajan, S.K. A review on the design and application of compliant mechanism-based fast-tool servos for ultraprecision machining. *Machines* **2023**, *11*, 450. [CrossRef]

9. Bingxiao, D.; Jiyu, Z.; Li, Y. Design of a spatial constant-force end-effector for polishing/deburring operations. *Int. J. Adv. Manuf. Technol.* **2021**, *116*, 3507–3515.

10. Bharanidaran, R.; Ramesh, T. A modified post-processing technique to design a compliant based microgripper with a plunger using topological optimization. *Int. J. Adv. Manuf. Technol.* **2017**, *93*, 103–112. [CrossRef]

11. Shan, Y.; Ding, B.; Zhong, J.; Li, Y. Design and optimization of a decoupled serial constant force microgripper for force sensitive objects manipulation. *Robotica* **2023**, *41*, 2064–2078. [CrossRef]

12. Ma, X.; Wilson, A.; Rahn, C.D.; Trolier-McKinstry, S. Efficient energy harvesting using piezoelectric compliant mechanisms: Theory and experiment. *J. Vib. Acoust.* **2016**, *138*, 021005. [CrossRef]

13. Le Chau, N.; Dang, M.P.; Prakash, C.; Buddhi, D.; Dao, T.P. Structural optimization of a rotary joint by hybrid method of FEM, neural-fuzzy and water cycle–moth flame algorithm for robotics and automation manufacturing. *Robot. Auton. Syst.* **2022**, *156*, 104199. [CrossRef]

14. Lyu, Z.; Xu, Q. Design of a new XY compliant parallel manipulator based on deployable spatial monolithic structure. *IEEE ASME Trans. Mechatron.* **2024**, *29*, 3762–3773. [CrossRef]

15. Zhu, J.; Hao, G.; Li, S.; Kong, X. A compact mirror-symmetrical XY compliant parallel manipulator for minimizing parasitic rotations. *J. Mech. Des.* **2022**, *144*, 073303. [CrossRef]

16. Ding, B.; Yang, Z.; Li, Y. Design of flexure-based modular architecture micro-positioning stage. *Microsyst. Technol.* **2020**, *26*, 2893–2901. [CrossRef]

17. Ding, B.; Li, X.; Li, C.; Li, Y.; Chen, S.C. A survey on the mechanical design for piezo-actuated compliant micro-positioning stages. *Rev. Sci. Instrum.* **2023**, *94*, 101502. [CrossRef]

18. Nohava, J.; Randall, N.X.; Conté, N. Novel ultra nanoindentation method with extremely low thermal drift: Principle and experimental results. *J. Mater. Res.* **2009**, *24*, 873–882. [CrossRef]

19. Hu, Z.; Lynne, K.J.; Markondapatnaikuni, S.P.; Delfanian, F. Material elastic–plastic property characterization by nanoindentation testing coupled with computer modeling. *Mater. Sci. Eng. A* **2013**, *587*, 268–282. [CrossRef]

20. Wu, Z.; Xu, Q. Survey on recent designs of compliant micro-/nano-positioning stages. *Actuators* **2018**, *7*, 5. [CrossRef]

21. Dang, M.P.; Le, H.G.; Tran, N.T.D.; Chau, N.L.; Dao, T.P. Optimal design and analysis for a new 1-DOF compliant stage based on additive manufacturing method for testing medical specimens. *Symmetry* **2022**, *14*, 1234. [CrossRef]

22. Wu, Z.; Li, Y.; Hu, M. Design and optimization of full decoupled micro/nano-positioning stage based on mathematical calculation. *Mech. Sci.* **2018**, *9*, 417–429. [CrossRef]

23. Dong, W.; Chen, F.; Gao, F.; Yang, M.; Sun, L.; Du, Z.; Tang, J.; Zhang, D. Development and analysis of a bridge-lever-type displacement amplifier based on hybrid flexure hinges. *Precis. Eng.* **2018**, *54*, 171–181. [CrossRef]

24. Yang, Y.; Wei, Y.; Lou, J.; Xie, F. Design and analysis of a new flexure-based XY stage. *J. Intell. Mater. Syst. Struct.* **2017**, *28*, 2388–2402. [CrossRef]

25. Wu, Z.; Xu, Q. Design, optimization and testing of a compact XY parallel nanopositioning stage with stacked structure. *Mech. Mach. Theory* **2018**, *126*, 171–188. [CrossRef]

26. Kim, H.Y.; Ahn, D.H.; Gweon, D.G. Development of a novel 3-degrees of freedom flexure based positioning system. *Rev. Sci. Instrum.* **2012**, *83*, 055114. [CrossRef]

27. Chen, X.; Li, Y. Design and analysis of a new high precision decoupled XY compact parallel micromanipulator. *Micromachines* **2017**, *8*, 82. [CrossRef]

28. Choi, S.B.; Han, S.S.; Han, Y.M.; Thompson, B.S. A magnification device for precision mechanisms featuring piezoactuators and flexure hinges: Design and experimental validation. *Mech. Mach. Theory* **2007**, *42*, 1184–1198. [CrossRef]

29. Yuan, L.; Ling, M.; Lai, J.; Li, H.; Zhang, X. Graphic transfer matrix method for kinetostatic and dynamic analyses of compliant mechanisms. *J. Mech. Robot.* **2024**, *16*, 021009. [CrossRef]

30. Wu, S.; Ling, M. A dynamic Timoshenko beam constraint model for use in compliant mechanisms with intermediate deformation ranges. *Precis. Eng.* **2025**, *94*, 447–460. [CrossRef]

31. Ling, M.; Howell, L.L.; Cao, J.; Chen, G. Kinetostatic and dynamic modeling of flexure-based compliant mechanisms: A survey. *Appl. Mech. Rev.* **2020**, *72*, 030802. [CrossRef]

32. Wang, H.; Zhang, X. Input coupling analysis and optimal design of a 3-DOF compliant micro-positioning stage. *Mech. Mach. Theory* **2008**, *43*, 400–410. [CrossRef]

33. Zhang, Q.; Zhao, J.; Shen, X.; Xiao, Q.; Huang, J.; Wang, Y. Design, modeling, and testing of a novel XY piezo-actuated compliant micro-positioning stage. *Micromachines* **2019**, *10*, 581. [CrossRef] [PubMed]

34. Wang, N.; Zhang, Z.; Zhang, X.; Cui, C. Optimization of a 2-DOF micro-positioning stage using corrugated flexure units. *Mech. Mach. Theory* **2018**, *121*, 683–696. [CrossRef]

35. Li, Y.; Wu, Z. Design, analysis and simulation of a novel 3-DOF translational micromanipulator based on the PRB model. *Mech. Mach. Theory* **2016**, *100*, 235–258. [CrossRef]

36. Zhao, H.; Huang, H.; Ji, J.; Ma, Z. Design and Analysis of Key Components in the Nanoindentation and Scratch Test Device. In *Human Musculoskeletal Biomechanics*; IntechOpen: London, UK, 2012.

37. Rabe, R.; Breguet, J.M.; Schwaller, P.; Stauss, S.; Haug, F.J.; Patscheider, J.; Michler, J. Observation of fracture and plastic deformation during indentation and scratching inside the scanning electron microscope. *Thin Solid Film.* **2004**, *469*, 206–213. [CrossRef]

38. Huang, H.; Zhao, H.; Ma, Z.; Hu, L.; Yang, J.; Shi, G.; Ni, C.; Pei, Z. Design and analysis of the precision-driven unit for nano-indentation and scratch test. *J. Manuf. Syst.* **2012**, *31*, 76–81. [CrossRef]

39. Huang, H.; Zhao, H.; Mi, J.; Yang, J.; Wan, S.; Xu, L.; Ma, Z. A novel and compact nanoindentation device for in situ nanoindentation tests inside the scanning electron microscope. *AIP Adv.* **2012**, *2*, 012104. [CrossRef]

40. Yang, X.S.; He, X. Firefly algorithm: Recent advances and applications. *Int. J. Swarm Intell.* **2013**, *1*, 36–50. [CrossRef]

41. Dang, M.P.; Le, H.G.; Chau, N.L.; Dao, T.P. Optimization for a Flexure Hinge Using an Effective Hybrid Approach of Fuzzy Logic and Moth-Flame Optimization Algorithm. *Math. Probl. Eng.* **2021**, *2021*, 6622655. [CrossRef]

42. Fan, W.; Jin, H.; Fu, Y.; Lin, Y. A type of symmetrical differential lever displacement amplification mechanism. *Mech. Ind.* **2021**, *22*, 5. [CrossRef]